PAPER • OPEN ACCESS

Low collisionality, peeling limited pedestals in JET-ILW: effect of density and isotope mass on pedestal structure, pedestal stability and pedestal prediction in deuterium and mixed deuterium/tritium plasmas

OPEN ACCESS
IOP Publishing | International Atomic Energy Agency
Nuclear Fusion
Nucl. Fusion 65 (2025) 076028 (31pp)
https://doi.org/10.1088/1741-4326/ade0d1

Low collisionality, peeling limited pedestals in JET-ILW: effect of density and isotope mass on pedestal structure, pedestal stability and pedestal prediction in deuterium and mixed deuterium/tritium plasmas

L. Frassinetti[1,*], D. King[2], S. Saarelma[2], D. Keeling[2], C. Perez von Thun[3], C. Giroud[2], S. Wiesen[4], A. Kappatou[5], N. Vianello[6], E. Alessi[7], M. Brix[2], I.S. Carvalho[8], P. Carvalho[2], A. Chomiczewska[3], J.M. Fontdecaba[9], E. Giovannozzi[10], D. Kos[2], E. Kowalska[3], B. Labit[11], M. Lennholm[2], M. Maslov[2], A. Meigs[2], S. Menmuir[2], R.B. Morales[2], H. Nyström[1], E. Pawelec[12], G. Pucella[10], D. Silvagni[5], A. Stagni[6], H.J. Sun[2], JET Contributors[a] and the EUROfusion Tokamak Exploitation Team[b]

EUROfusion Consortium, JET, Culham Science Centre, Abingdon OX14 3DB, United Kingdom of Great Britain and Northern Ireland

[1] Division of Electromagnetic Engineering and Fusion Science, KTH Royal Institute of Technology, Stockholm, Sweden
[2] UKAEA (United Kingdom Atomic Energy Authority), Culham Campus, Abingdon, Oxfordshire OX14 3DB, United Kingdom of Great Britain and Northern Ireland
[3] Institute of Plasma Physics and Laser Microfusion (IPPLM), Hery 23, 01-497 Warsaw, Poland
[4] DIFFER—Dutch Institute for Fundamental Energy Research, 5612 AJ Eindhoven, Netherlands
[5] Max-Planck-Institut für Plasma Physik, Boltzmannstr.2, 85748 Garching, Germany
[6] Consorzio RFX, Corso Stati Uniti 4, 35127 Padova, Italy
[7] Institute for Plasma Science and Technology, CNR, 20125 Milano, Italy
[8] ITER Organization, Route de Vinon-sur-Verdon, CS 90 046, 13067 St Paul Lez Durance Cedex, France
[9] Laboratorio Nacional de Fusión, CIEMAT, Madrid, Spain
[10] Fusion and Nuclear Safety Department—ENEA C. R. Frascati, Frascati (Roma), Italy
[11] Ecole Polytechnique Fédérale de Lausanne (EPFL), Swiss Plasma Center (SPC), Lausanne, Switzerland
[12] Institute of Physics, University of Opole, Opole, Poland

[a] See Maggi *et al* 2024 (https://doi.org/10.1088/1741-4326/ad3e16) for JET Contributors.
[b] See Joffrin *et al* 2024 (https://doi.org/10.1088/1741-4326/ad2be4) for the EUROfusion Tokamak Exploitation Team.
* Author to whom any correspondence should be addressed.

E-mail: lorenzof@kth.se

Received 14 February 2025, revised 2 June 2025
Accepted for publication 4 June 2025
Published 17 June 2025

Abstract

Pedestals limited by peeling instabilities have been reached in JET-ILW by operating at high q_{95}, up to $q_{95} = 8.5$. The increase in q_{95} via the increase of the toroidal field has stabilized the ballooning modes and has allowed to reach high pedestal temperature (up to 1.5 keV for the electrons and up to 2.2 keV for the ions) and low pedestal density ($\approx 1.8 \times 10^{19}\mathrm{m}^{-3}$), with electron–electron pedestal collisionality approximately 0.15 and normalized ion Larmor radius 0.002 approaching ITER normalized pedestal parameters. The most unstable pedestal instabilities are peeling with toroidal mode numbers in the range $n = 1-5$. A density scan in peeling limited pedestals shows that the increase of the pedestal density leads to an increase in the pedestal pressure. The modeling shows that this effect is due to the stabilizing effect of the density on the peeling modes. On the contrary, the increase of the separatrix density does not seem to affect the pedestal pressure in peeling limited plasmas. These behaviors are opposite to those observed in ballooning limited pedestals. An isotope mass scan from pure deuterium to tritium-rich plasmas has been performed with peeling limited pedestals. The increase of the isotope mass leads to an increase of the density at the pedestal top, via the increase of the density gradient. This behavior is similar to that observed in ballooning limited pedestals. The increase of the isotope mass also leads to the increase of the pressure at the pedestal top, via the increase in the pressure gradient. The temperature is not affected significantly. The increase in the pressure is not ascribed to a direct effect of the isotope mass on the pedestal stability, but to an indirect effect due to the increase of the pedestal density which, as shown in the deuterium density scan, stabilizes the peeling modes. The experimental results are used to validate the pedestal predictions using the Europed code. In all the scans performed, a good qualitative agreement is observed between the predictions and the experimental results. Quantitative disagreements can be in part ascribed to the fact that a consistent modeling should integrate the effect of core and scrape-off layer.

Keywords: pedestal, JET-ILW, peeling, isotope mass, pedestal stability, pedestal structure, Europed

(Some figures may appear in colour only in the online journal)

1. Introduction

ITER fusion performance is expected to increase strongly with the increase of the pedestal pressure [1], due to the coupling between core and pedestal. To reach $Q = 10$ (where Q is the ratio between the fusion power and the input power), a pedestal temperature $T^{\mathrm{ped}} \approx 4-5\mathrm{keV}$ has been estimated for ITER [1–3]. This estimation has been strengthened in past 10–15 years by modeling and predictive simulations [4–8]. At this temperature, the ITER pedestal is expected to have collisionality $\nu_e^{*\mathrm{ped}} \lesssim 0.1$. In H-mode plasmas, the pedestal is limited by edge localized modes (ELMs) that are triggered by MHD instabilities. The edge instabilities that affect the pedestal are the ballooning modes (typically characterized by high toroidal mode numbers, $n \gtrsim 15-20$), the peeling modes, (typically characterized by low n, $n \lesssim 10$) and the coupled peeling-ballooning modes (characterized by intermediate-high n). An assessment of the pedestal instabilities in ITER has been performed in several works. For example, [9] shows that, in an ITER scenario, the peeling instabilities are very sensitive to the current density at the separatrix and that a good model for the pedestal bootstrap current is necessary to reliably predict the limiting instability of ITER pedestals. More recent predictive analysis with the EPED code suggest that ITER will be limited by peeling instabilities [10]. As shown also in a set of pedestal stability analysis for the ITER baseline scenario, the main pedestal instability in ITER can have toroidal harmonic as low as $n = 1$ [7]. Therefore, pedestal physics studies in low n peeling limited plasmas have high priority. In particular, validating pedestal predictions in these conditions is essential to strengthen and improve ITER predictions.

Pedestals limited by peeling modes have been achieved so far only in DIII-D [10–13], in some in NSTX pulses [14–17] and in some Alcator C-mod pulses performed at low density to reach the super H-mode scenario [18]. Peeling limited pedestals have been seen for short time intervals also in European machines in the brief naturally ELM-free quiescent H-mode (QH-mode), as shown for example in AUG [19]. Unfortunately, until recently, all other machines have not been able to reach stationary plasmas limited by peeling instabilities. Examples are JET with the carbon wall (JET-C) [20–22], AUG [23, 24], TCV [25, 26], MAST [27–29], JT-60 U [30] and most of the Alcator C-mod scenarios [15, 31, 32], where the pedestal is limited by coupled peeling-ballooning modes. Also JET with the ITER-like wall (JET-ILW) has so far obtained only plasmas with the pedestal limited by ballooning instabilities [33–40]).

The pedestal behavior strongly depends on the limiting edge instability. Pedestals limited by peeling modes are expected to have an increasing pedestal pressure (p^{ped}) with increasing pedestal density (n^{ped}) and with increasing separatrix density (n^{sep}). This has been observed and modeled in DIII-D [10]. Plasmas limited by ballooning modes are characterized by a decreasing pedestal pressure with increasing n^{ped} [3, 20, 23, 35, 41] and by a clear degradation of the pedestal performance with increasing n^{sep} [23, 25, 26, 40–42]. Understanding the pedestal physics in peeling limited plasmas, experimentally confirming the different pedestal behaviors between peeling and ballooning limited plasmas and validating the pedestal predictions are important studies in view of ITER. In particular, since ITER will operate at high n^{sep} [43] and in mixed deuterium/tritium plasmas, assessing the role of n^{sep} and of the isotope mass in peeling limited plasmas and in a metal wall machine is essential to guarantee a high ITER pedestal performance.

In the most recent years, a significant effort has been devoted to reach peeling limited pedestals in European machines in order to (1) understand if peeling limited pedestals can be reached in metal wall machines, (2) study pedestal physics and (3) validate pedestal predictions in ITER-relevant conditions. In MAST-U, peeling limited pedestal have been achieved via a plasma shape effect and operating at low collisionality [44]. Promising preliminary results for TCV, MAST-U and JET-ILW have been presented in recent conferences [45, 46]. This work presents an in depth analysis of the recently achieved peeling limited scenario in JET-ILW, with emphasis on pedestal structure, pedestal stability and validation of pedestal predictions. The goals of the work are to (1) test a strategy to reach peeling limited pedestals in JET-ILW, (2) experimentally assess the correlation between p^{ped} and n^{ped} and between p^{ped} and n^{sep} in JET-ILW peeling limited plasmas, (3) assess the role of the isotope mass on the pedestal in JET-ILW peeling limited plasmas (in deuterium, mixed deuterium/tritium plasma and tritium-rich plasmas) and (4) validate the pedestal predictions.

The work is organized as follow. Section 2 describes the key diagnostics, the data analysis technique, the modeling tools and the datasets used. Section 3 presents the strategy used to reach low collisionality, peeling limited pedestals in JET-ILW and compares the experimental results with the pedestal predictions. Section 4 presents the correlation between pedestal pressure and pedestal density in low collisionality, peeling limited plasmas and compares the experimental trends with the predicted trends. Section 5 presents the effect of the separatrix density on the pedestal in peeling limited plasmas and compares the results with the modeling and with earlier ballooning limited datasets. Section 6 describes the effect of the isotope mass, from pure deuterium plasmas to tritium-rich plasmas. Finally, section 7 presents the discussion and section 8 presents the conclusions. appendix A presents the behavior of the ion temperature in the main datasets. appendix B shows sensitivity tests of relevant input parameters on the pedestal predictions. appendix C shows the 2D radial displacement reconstructed from the profile of the eigenfunctions of the most unstable pedestal modes for some specific cases.

2. Diagnostics, experimental data analysis technique, modeling tools and datasets

This section will describe the pedestal diagnostics used, the method to process the experimental data, the numerical tools for the pedestal stability and for the pedestal predictions and the datasets used.

2.1. Diagnostics

To quantify in the best way possible the pedestal structure, all the available diagnostics to measure electron temperature profile (T_e), electron density profile (n_e) and ion temperature profile (T_i) are used. The majority of the earlier studies in the JET pedestals have used only the Thomson scattering, so the present work has very high quality pedestal data.

The high resolution Thomson scattering (HRTS) measures both T_e and n_e profiles at 20 Hz [47]. The electron temperature profiles have been measured also using the electron cyclotron emission diagnostic (ECE) [48] which has a high time resolution (2.5 kHz in the dataset of this work) but can measure only until the top/middle of the pedestal in the datasets used in this work. The electron density has been measured also with the lithium beam and the reflectometry. For the present dataset, the Lithium beam [49] provides high quality profiles in the scrape off layer (SOL) at 100 Hz but does not reach the pedestal top while the reflectometer [50] covers the whole pedestal region and has a 400 Hz time resolution. The ion temperature has been measured with the core and edge charge exchange spectroscopy (CXRS), providing T_i of the main impurity (neon, since trace neon puffs have been used explicitly to measure T_i) at 33 Hz and 20 Hz time resolution respectively. An overview of the T_i behavior for the main datasets discussed in this work is presented in appendix A. The effective mass has been measured from the sub-divertor neutral gas pressure via spectral analysis of D_α and T_α emission from a Penning gauge. Despite being measured in the sub-divertor, this measurement agrees well with that from spectroscopy at the plasma edge and is consistent with the core isotope ratio modeled with TRANSP within 5% [51, 52]. The effective mass has been defined as: $A_{eff} = (c_H A_H + c_D A_D + c_T A_T)/(c_H + c_D + c_T)$ where A_H, A_D, A_T are the relative atomic mass $A_i = m_i/m_p$ of hydrogen, deuterium and tritium respectively and c_H, c_D, c_T are the concentrations of H, D, T. Z_{eff} is a line averaged value and is measured by visible Bremsstrahlung and no profiles are available for this dataset. Unfortunately, the uncertainty in Z_{eff} is very large. Therefore, the value $Z_{eff} = 1.5$ has been assumed. This value is consistent with earlier measurements in JET-ILW unseeded plasmas. In appendix B, a sensitivity test shows that the value of Z_{eff} cannot affect the qualitative conclusions of this work.

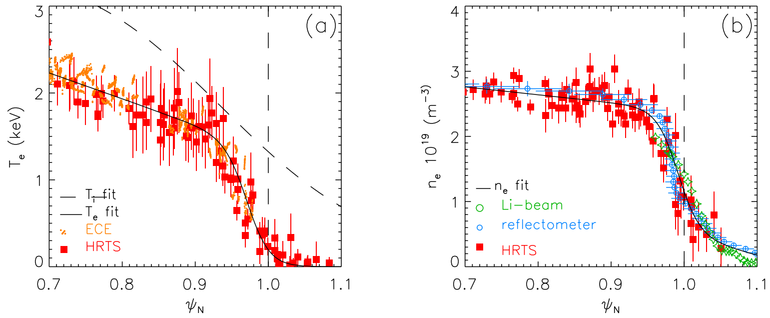

Figure 1. Pre-ELM profiles for the deuterium pulse #103 798. Frame (*a*) shows the electron temperature measured from HRTS (red squares) and ECE (orange dots). Frame (*b*) shows the electron density measured from HRTS (red squares) reflectometry (blue circles) and Li-beam (green diamonds). Frame (*c*) shows the pre-ELM ion temperature profile. The continuous black lines are the corresponding mtanh fits. In frame (*a*), the $T_{\rm i}$ fit is shown to provide a direct comparison with the $T_{\rm e}$ profile.

2.2. Data analysis technique

The present work describes the pedestal structure before the ELMs are triggered. The reason is to have a direct comparison with the pedestal stability and the pedestal predictions.

To extract information of the pedestal structure, only stationary time windows at least 2 energy confinement time long have been considered. Within these time windows, the pre-ELM profiles have been defined, as in all earlier JET-ILW works, as those located in the 70%–99% of the ELM cycle (when the profiles are approximately stationary) [53]. A wider pre-ELM range would include profiles that are still significantly recovering from the ELM crash and a narrower pre-ELM range might not contain enough experimental data point for a careful characterization of the pedestal structure. The profiles are then mapped on the normalized poloidal flux coordinate $\psi_{\rm N}$ using the best available equilibrium from EFIT++ (determined with the full set of available magnetic measurements [54]). The pre-ELM selected HRTS and ECE profiles provide a combined experimental pre-ELM $T_{\rm e}$ profile. The pre-ELM selected HRTS, Li-beam and reflectometer profiles provide a combined pre-ELM $n_{\rm e}$ profile. The CXRS provides the pre-ELM $T_{\rm i}$ profile. The experimental profiles are then fitted using the modified hyperbolic tangent function (mtanh) [55] with a SOL slope added for the density [56]. An example of the pre-ELM profiles and the corresponding fits, for a plasma discussed in this work, is shown in figure 1. Note that the ion temperature at the separatrix $\left(T_{\rm i}^{\rm sep}\right)$ is significantly higher than the electron temperature at the separatrix $\left(T_{\rm e}^{\rm sep}\right)$. The very high $T_{\rm i}^{\rm sep}$ might be due to the fact that the impurity temperature at the separatrix can be higher than the main ion temperature, as discussed for example in DIII-D [57]. For this reason, appendix B presents a wide sensitivity test on the effect of $T_{\rm i}^{\rm sep}/T_{\rm e}^{\rm sep}$, showing that the conclusions of the present work are not affected by the ratio $T_{\rm i}^{\rm sep}/T_{\rm e}^{\rm sep}$.

Finally, to minimize possible uncertainties related to the equilibrium, the experimental $T_{\rm e}$ pre-ELM profiles and the fits are radially shifted in order to have a specific temperature at the separatrix. The same radial shift is also applied to the density profile. In all earlier works, this procedure was applied assuming systematically $T_{\rm e}^{\rm sep} = 100\,{\rm eV}$ (estimated from the

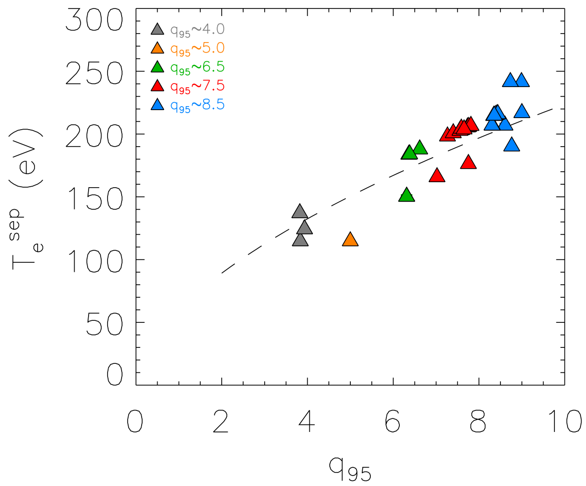

Figure 2. Separatrix temperature versus q_{95} determined with the two-point-model for the dataset described in section 3. The dashed line shows the trend $T_{\rm e}^{\rm sep} \sim (q_{95})^{4/7}$ expected from the two-point model. The colors highlight the different $B_{\rm t}$ and q_{95}.

two-point-model [58]) since it was shown that a reasonable uncertainty in $T_{\rm e}^{\rm sep}$ would not have affected significantly any result. However, the separatrix temperature in the two-point-model has a dependence on q_{95} via the connection length. As described in the next section, most of the plasmas discussed in this work have q_{95} significantly higher than the usual JET scenarios, so in this work the 100 eV assumption has not been used. For each shot, $T_{\rm e}^{\rm sep}$ has been determined with the two-point-model using the approach described in [59]. The corresponding $T_{\rm e}^{\rm sep}$ is shown in figure 2 for the dataset discussed in section 3. Indeed, $T_{\rm e}^{\rm sep} \approx 100-120\,{\rm eV}$ in the usual JET q_{95} range (3–4) while it increases up to $T_{\rm e}^{\rm sep} \approx 200-250\,{\rm eV}$ at $q_{95} \approx 8.5$. The dashed line shows the expected trend from the two point model. Using $T_{\rm e}^{\rm sep} \approx 200\,{\rm eV}$ instead of 100 eV has a small but not negligible effect on the pedestal stability due to the change in the pedestal position [26].

The electron–electron pedestal collisionality $\nu_{\rm ee}^{*\rm ped}$ and normalized ion Larmor $\rho_i{}^{*\rm ped}$ are calculated from the fits to the pre-ELM experimental profiles and are defined as:

$$\nu_{ee}{}^{*\mathrm{ped}} = 6.921\cdot 10^{-18}\ln\Lambda \frac{Rq_{95}n_{\mathrm{e}}^{\mathrm{ped}}}{\varepsilon^{3/2}\left(T_{\mathrm{e}}^{\mathrm{ped}}\right)^{2}}$$

$$\text{with } \ln\Lambda = 31.3 - \ln\frac{\sqrt{n_{\mathrm{e}}^{\mathrm{ped}}}}{T_{\mathrm{e}}^{\mathrm{ped}}} \quad (1)$$

$$\rho_i{}^{*\mathrm{ped}} = \frac{\sqrt{2m_{\mathrm{i}}T_{\mathrm{i}}^{\mathrm{ped}}}}{\sqrt{e}Ba} \quad (2)$$

where $\varepsilon = a/R$ (being a and R the minor and major radius respectively) and where the density is expressed in m^{-3} and the temperature in eV, m_{i} is the ion mass in kg, e is the electron charge in *Coulomb* and the total magnetic field on axis is in *Tesla*.

2.3. Modeling tools

The pedestal stability analysis has been performed using as input parameters the fit to the experimental pre-ELM profiles (section 2.2) including the experimental ion temperature and using the separatrix temperature determined from the two-point model. The ion density is determined from the electron density and Z_{eff}, assuming beryllium as main impurity.

The equilibrium is determined using the standard JET approach with HELENA [60], a fixed boundary equilibrium solver that takes in input the fit to the experimental data of both electron and ion pressure profiles. The HELENA equilibrium provides a total pressure profile that satisfies $p_{\mathrm{tot}} \geqslant p_{\mathrm{e}} + p_{\mathrm{i}}$ everywhere. The bootstrap current j_{bs} has been determined with the Redl formula [61].

The pedestal stability is calculated with MISHKA, a linear ideal MHD stability code [62]. MISHKA determines the ideal stability of peeling, ballooning and coupled peeling-ballooning modes in the $j-\alpha$ space, where j is the current density (composed of the fully diffused Ohmic current and the bootstrap current j_{bs}) and α is the normalized pressure gradient defined as in [63];

$$\alpha = -\frac{2\partial_{\psi}V}{(2\pi)^2}\left(\frac{V}{2\pi^2 R}\right)^{1/2}\mu_0 p' \quad (3)$$

where V is the plasma volume enclosed by the flux surface, R is the major radius and p' is the total pressure derivative in the poloidal flux Ψ. The stability threshold has been defined by using the diamagnetic criterion applying the bilinear model [6, 64]. The diamagnetic criterion has been selected because of its dependence on the isotope mass A which can potentially explain the effect of the isotope on the pedestal stability (for details, see [65, 66] and section 6). The bilinear model assumes the stability threshold is at $\gamma_n/\omega^{*n}_{\mathrm{max}} = 0.25$ for $n \leqslant 10$ (where γ_n is the growth rate of the instability with toroidal harmonic n and $\omega^{*n}_{\mathrm{max}}$ is the corresponding maximum diamagnetic frequency in the pedestal for the harmonic n) and at $\gamma_n/\omega^{*n=10}_{\mathrm{max}} = 0.25$ for $n > 10$, similarly to what used in ELITE calculations. The choice $n = 10$ was motivated by earlier BOUT++ simulations [6, 67, 68]. However, as discussed in [6], the use of the bilinear model does not have a major effect in large tokamaks and at low collisionality. So, the present results are not sensitive to the exact choice of $n = 10$. In the stability calculation, the following toroidal harmonics have been included: $n = 1$, 2, 3, 5, 7, 10, 20, 30, 50, to cover a range from peeling modes to ballooning modes. The stability analysis with MISHKA has assumed a perfectly conducting wall located at $R_{\mathrm{wall}}/a = 10$, like usually done in all previous works. A sensitivity test has verified that the decrease to $R_{\mathrm{wall}}/a = 1.2$ does not lead to any significant variation in the growth rates of the low n modes and does not affect the Europed pedestal predictions.

The pedestal predictions have been performed with the Europed code [64, 67] which implements the EPED1 model [4]. The code creates a set of profiles assuming that the pedestal widths of temperature and density are equal and are determined via the expression:

$$w = 0.076\sqrt{\beta_{\theta}^{\mathrm{ped}}} \quad (4)$$

where $\beta_{\theta}^{\mathrm{ped}}$ is the polodal beta at the pedestal top. The prediction is the profile marginally stable to peeling-ballooning modes. In the version used in this work, the key input parameters are the plasma current I_{p}, the toroidal magnetic field B_{t}, the plasma shape, the normalized pressure β_{N}, the effective charge Z_{eff}, the separatrix temperature $T_{\mathrm{e}}{}^{\mathrm{sep}}$, the electron density at the pedestal top $n_{\mathrm{e}}^{\mathrm{ped}}$, the ratio between ion and electron temperature and the relative shift (defined as $n_{\mathrm{e}}^{\mathrm{pos}} - T_{\mathrm{e}}^{\mathrm{pos}}$, where $T_{\mathrm{e}}^{\mathrm{pos}}$ is the position of the pedestal temperature and $n_{\mathrm{e}}^{\mathrm{pos}}$ is the position of the pedestal density). In Europed, $T_{\mathrm{e}}^{\mathrm{pos}}$ is determined via the boundary condition $T_{\mathrm{e}}{}^{\mathrm{sep}}$, while $n_{\mathrm{e}}^{\mathrm{pos}}$ is determined via the relative shift. The equilibrium is determined with HELENA, the stability with MISHKA using $n = 1$, 2, 3, 5, 7, 10, 20, 30, 50 and the diamagnetic criterion. Given that the ratio $T_{\mathrm{i}}/T_{\mathrm{e}}$ is an input parameter, all pedestal predictions are discussed only in terms of electron pressure. A sensitivity test of the effect of $T_{\mathrm{i}}/T_{\mathrm{e}}$ on the pedestal predictions is discussed in appendix B.

2.4. Datasets

The main experimental datasets are a specific new set of experiments performed in the years 2022–23 with the goal of reaching peeling limited pedestals in JET-ILW. Hereafter, these new datasets are called the main datasets (datasets 1–7 in table 1). To reach peeling limited pedestals, a unique set of engineering parameters has been explored (i.e. high q_{95}, see section 3). The main datasets are composed of a q_{95} scan at 1.4 MA, with 25 MW of auxiliary power P_{aux} (defined as $P_{\mathrm{aux}} = P_{\mathrm{NBI}} + P_{\mathrm{ICRH}}$) and at high triangularity. Datasets 4 and 5, at $q_{95} = 7.5$ and 8.5 respectively, have also a gas rate scan. Datasets 6 and 7 are gas rate scans at $q_{95} = 8.5$ in mixed deuterium/tritium plasmas and tritium-rich plasmas respectively. A subset of datasets 1–5 selected at similar gas rate will be used in section 3 to discuss the q_{95} scan. Dataset 5 will be used in section 4 to discuss the $n_{\mathrm{e}}^{\mathrm{ped}}$ scan in peeling limited pedestals. A subset of dataset 5 at constant $n_{\mathrm{e}}^{\mathrm{ped}}$ will be used

Table 1. Summary of the engineering parameters for the datasets used in this work. In the first column, the label 'main' identifies the main datasets, the label 'comp' identifies earlier datasets used for comparison with the main ones.

Dataset	I_p (MA)	B_t (T)	q_{95}	$<\delta>$	P_{aux} (MW)	Γ_D 10^{22}(e/s)	A_{eff}	Symbols/colors color	References
1 (main)	1.4	1.7	4.0	0.38	25	0.8–1.0	2.0	Full triangles/grey	
2 (main)	1.4	2.2	5.0	0.38	25	0.6–0.8	2.0	Full triangles/orange	
3 (main)	1.4	2.8	6.5	0.38	25	0.2–0.6	2.0	Full triangles/green	
4 (main)	1.4	3.4	7.5	0.38	25	0.2–0.9	2.0	Full triangles/red	
5 (main)	1.4	3.8	8.5	0.38	25	0.0–0.8	2.0	Full triangles/blue	
6 (main)	1.4	3.8	8.5	0.38	25	0.0–0.8	2.5	Full triangles/gold	
7 (main)	1.4	3.8	8.5	0.38	25	0.0–0.8	2.9	Full triangles/magenta	
8 (comp)	1.4	1.7	4.0	0.38	6–16	0.3	2.0	Empty squares/grey	[69]
9 (comp)	2.5	2.7	3.5	0.38	16	0.7–3.0	2.0	Empty inverted triangles /grey	[70]
10 (comp)	2.0	2.3	3.5	0.23	12	0.4–6.0	2.0	Empty stars/grey	[40]
11 (comp)	1.4–2.5	1.7–3.4	3.0–4.5	0.33–0.38	8–30	0.3–20.0	2.0	Empty small triangles/grey	[42]
12 (comp)	2.0	2.3	3.5	0.23	10–15	1.7	2.0–3.0	Empty thick circles/blue, gold, magenta	[66]

in section 5 to discuss the role of n_e^{sep} in peeling limited pedestals. Datasets 6 and 7 will be used in section 6 to discuss the effect of the isotope mass in peeling limited pedestals.

Throughout the paper, the main datasets are compared with earlier published JET-ILW datasets limited by ballooning modes. Due to the unique engineering parameters of the main datasets, it impossible to find earlier pulses fully consistent with the main datasets. So, the comparison is only qualitative to highlight the different behavior between peeling limited pedestals and ballooning limited pedestals.

In section 3, the 1.4 MA, high-δ, q_{95} scan datasets are compared with an earlier power scan at 1.4 MA/1.7 T, $q_{95} = 4.0$, high-δ (dataset 8) to highlight the different pedestal behavior in a q_{95} scan and in a power scan. Dataset 8 is described in details in [35, 69].

In section 4, the gas scan at $q_{95} = 8.5$ (dataset 5) is compared with a gas scan at 2.5 MA/2.7 T/ $q_{95} = 3.5$ in high triangularity/high collisionality plasmas (dataset 9). Dataset 9 is described in in [70].

In section 5, the separatrix density scan is compared with the earlier results in ballooning limited pedestals at 2 MA/2.3 T/$q_{95} = 3.5$/low triangularity (dataset 10). Dataset 10 is described in [40].

In section 6, the isotope mass scan is compared with the recent results in ballooning limited pedestals at 2 MA/2.3 T/ $q_{95} = 3.5$/low triangularity (dataset 12). Dataset 12 is described in [66].

To compare the parameters space between the main datasets and earlier results, dataset 11 is used. Dataset 11 covers all the high triangularity JET-ILW plasmas without seeding obtained until 2020 (see [42]). Dataset 11 is used in several sections throughout the paper.

All datasets are from JET-ILW. Comparison with JET-C will be a future work. All datasets are type I ELMy H-modes (see [42]).

Unless otherwise stated, the datasets are in pure deuterium plasmas. Dataset 6 is 50% deuterium and 50% tritium. Dataset 7 is with tritium-rich plasmas. The isotope composition will be discussed in detail in section 6.

The engineering parameters I_p, B_t, q_{95}, average triangularity $\langle\delta\rangle$, P_{aux}, gas rate Γ_D and effective isotope mass A_{eff} are summarized in table 1. Pedestal normalized collisionality ν_{ee}^{*ped}, pedestal normalized ion Larmor radius ρ_i^{*ped}, Troyon beta limit β_N, poloidal normalized pressure β_{pol} and type of pedestal instabilities are summarized in table 2. The effective mass , the pedestal collisionality and the normalized pedestal ion Larmor radius are defined in sections 2.1 and 2.2.

The main datasets are highlighted with full triangles throughout the paper. The earlier datasets used for comparison are highlighted with empty grey symbols. Predictive Europed modeling is highlighted with empty symbols linked via a continuous line.

3. Reaching peeling limited pedestals: q_{95} scan

JET-ILW has so far not reached plasmas with the pedestal limited by peeling instabilities. Even at low collisionality in the hybrid scenario, the pedestal was at the ballooning boundary limited by ballooning modes or coupled peeling-ballooning modes with medium-high n ($n > 10$) [35, 71]. An extensive study using the EUROfusion pedestal database [42] has not identified any peeling limited pedestal in JET-ILW. This section describes a strategy to reach peeling limited pedestals in JET-ILW and the corresponding results.

Datasets used. A subset of datasets 1–5 selected with gas rate as constant as possible has been used. The subset represents a q_{95} scan at constant I_p, input power and gas rate in deuterium high-triangularity plasmas. The subset is compared with dataset 8 (power scan in deuterium high-triangularity plasmas with same I_p as the main datasets) and dataset 11 (all JET-ILW high-triangularity plasmas until 2020) to provide a qualitative comparison with ballooning limited plasmas.

3.1. The strategy to reach peeling limited pedestals

Europed has been applied to a low collisionality JET-ILW pulse and predictive simulations have been used to test if peeling limited pedestals can be reached by decreasing the collisionality either via a decrease in density and/or via an increase in temperature (by increasing the Europed input parameter β_N). Within the experimentally achievable ranges of n_e^{ped}

Table 2. Summary of plasma parameters for the datasets used in this work with normalized electron-electron pedestal collisionality, normalized ion Larmor radius, global normalized β, global poloidal β and type of pedestal instabilities (determined from peeling ballooning stability analysis).

Dataset	$\nu^{*}{}_{ee}{}^{ped}$	$\rho^{*\,ped}$ x 100	β_N	β_{pol}	Pedestal instabilities
1 (main)	0.21–0.40	0.38–0.43	3.0–3.2	1.3–1.4	$n = 20$–40
2 (main)	0.31–0.31	0.34–0.35	2.9–3.0	1.6–1.6	$n = 20$–30
3 (main)	0.24–0.34	0.25–0.27	1.8–2.3	1.3–1.6	$n = 10$–20
4 (main)	0.23–0.39	0.21–0.23	1.6–1.9	1.3–1.6	$n = 5$–15
5 (main)	0.15–0.25	0.18–0.20	1.4–1.7	1.3–1.7	$n < 10$
6 (main)	0.18–0.28	0.21–0.22	1.6–1.8	1.5–1.7	$n < 10$
7 (main)	0.18–0.29	0.20–0.22	1.5–1.8	1.5–1.7	$n < 10$
8 (comp)	0.40–1.75	0.25–0.40	1.5–3.0	0.7–1.3	$n = 30$–50
9 (comp)	0.73–1.56	0.19–0.23	1.2–1.6	1.0–1.6	$n = 30$–50
10 (comp)	0.65–2.80	0.17–0.23	1.1–1.3	0.5–0.6	$n = 30$–50
11 (comp)	0.37–4.0	0.15–0.40	1.0–3.2	0.3–1.3	$n = 30$–50
12 (comp)	0.70–1.8	0.20–0.22	1.45–1.55	0.55–0.65	$n = 30$–50

and β_N, Europed predicts that the peeling boundary cannot be reached starting from an existing JET-ILW pulse. Since the increase in the toroidal field stabilizes the ballooning modes, the Europed predictions have been extended to high B_t. Starting from an existing scenario at low density, high power, 1.4 MA/1.7 T [69], Europed has been used to predict the pedestal in a B_t scan at constant I_p. The predictions show that above $B_t \approx 3.5T - 3.6T$, the peeling boundary can be reached.

The rest of the section describes the experimental results of a q_{95} scan obtained via a B_t scan at constant I_p and constant power performed with the goal of reaching peeling limited pedestals in JET-ILW. To prioritize the experimental results and to have a direct validation, the pedestal predictions are presented only in the context of the experimental data and are discussed at the end of the section.

3.2. The plasma scenario at high q_{95}

The scenario has been chosen to have density as low as possible and power as high as possible. This has been done by operating at low current ($I_p = 1.4$MA), with the strike points in the corner configuration (near the vacuum pump duct), at low gas rate with $\Gamma_D = 0.5 - 0.8 \times 10^{22}\left(\mathrm{e\,s^{-1}}\right)$ and with the maximum possible input power. In the achieved density range, the maximum power compatible with no shine-through and no reionization issues is approximately $P_{aux} = 25$MW composed of $P_{NBI} = 22 - 23$MW and $P_{ICRH} = 2 - 3$MW (for tungsten control). In some pulses, for technical reasons only NBI heating has been used to reach $P_{aux} = 25$MW. To be ITER relevant, the high triangularity shape has been used (despite this can lead to higher density) with average triangularity $\langle\delta\rangle = 0.38$.

The toroidal field has been changed shot by shot from $B_t = 1.7$T (corresponding to $q_{95} \approx 4.0$) to $B_t = 3.8$T ($q_{95} \approx 8.5$). An example of key time traces for pulse #103708 at 1.4 MA/3.8 T is shown in figure 3. The plasma enters H-mode at 46.5 s when the NBI power exceeds 10–14 MW. The plasma is characterized by type III ELMs with high ELM frequency ($f_{ELM} \approx 60 - 70$Hz) until 47.1 s. The increase of the NBI power above 20 MW leads to the transition from type III to type I ELMs, characterized by $f_{ELM} \approx 10 - 20$Hz. The final power increase at 48 s leads to an increase in the ELM frequency to $f_{ELM} \approx 30 - 40$Hz. The increase of f_{ELM} with increasing power is a clear signature of type I ELMs [72]. Since the power is significantly higher than the P_{LH} threshold and f_{ELM} increases with power, the ELMs considered in this work are type I. The ELM energy losses are in the range $\Delta W_{ELM}/W_{ped} \approx 10\% - 15\%$, a value compatible with type I ELMs [73].

The dataset used in this work considers only time intervals at $P_{aux} = 25$MW. So, for the example of figure 3, only the pre-ELM data between 48 s and 49.3 s are considered.

3.3. Pedestal structure in the q_{95} scan

The pre-ELM T_e^{ped} and n_e^{ped} of the q_{95} scan are shown in figure 4 with full triangles. The increasing q_{95} via the increasing B_t leads to a clear reduction in n_e^{ped} and a clear increase in T_e^{ped}. The reduction in n_e^{ped} with increasing B_t is qualitatively similar to earlier results obtained both in Alcator C-mod [74] and JET [75]. The pedestal pressure remains constant. The pedestal ion temperature shows a qualitatively similar behavior to T_e^{ped} while quantitatively T_i^{ped} is roughly 20% higher than T_e^{ped} (see appendix A). For reference, figures 4(*a*)–(*c*) display with empty squares an earlier NBI power scan (dataset 8) in 1.4 MA/1.7 T high-δ plasmas [69]. The increase in q_{95} is able to increase T_e^{ped} and to decrease n_e^{ped} to values not reached in dataset 8.

At high q_{95}, the pedestal approaches dimensionless parameters much closer to the ITER range then in the standard $q_{95} = 4.0$ scenario, as shown in figure 4(*d*). In the earlier power scan [69] (dataset 8), the lowest collisionality was $\nu_{ee}^{*ped} \approx 0.4$ and the corresponding normalized Larmor radius $\rho_i{}^{*ped} \approx 0.004$. The present q_{95} scan reaches lower collisionality, $\nu_{ee}^{*ped} \approx 0.15$, (due to both the reduction in n_e^{ped} and the increase in T_e^{ped} and despite the q_{95} increase) and lower Larmor radius to $\rho_i^{*ped} \approx 0.002$ (due to the increase in B_t) therefore starting to approach the ITER range.

For completeness, figures 4(*e*) and (*f*) compare the q_{95} scan dataset with dataset 11 (which includes all JET-ILW high triangularity pulses until 2020). The q_{95} scan dataset reaches ranges

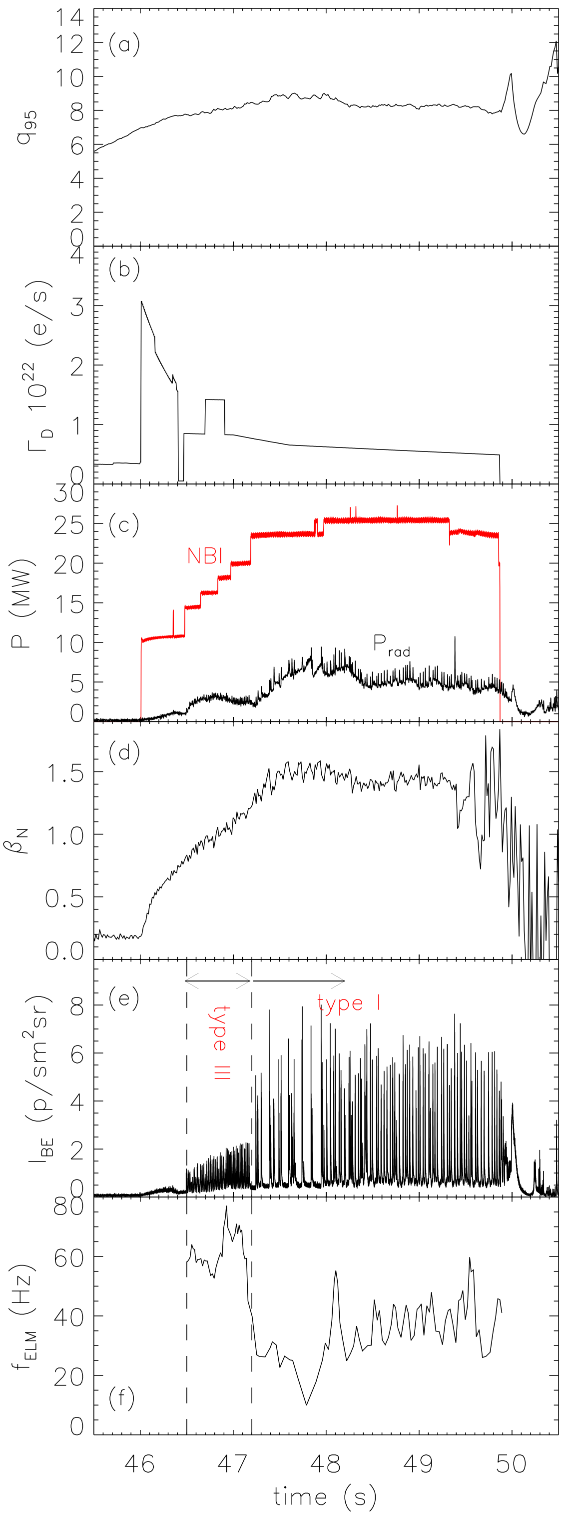

Figure 3. Time traces for #103708 at 1.4 MA/3.8 T showing q_{95} in frame (*a*), deuterium gas rate (*b*), NBI power in red and the power radiated by the bulk plasma in black (*c*), β_N (*d*), beryllium light as ELMs marker (*e*) and ELM frequency (*f*).

in T_e^{ped} and n_e^{ped} never obtained in earlier high triangularity JET-ILW pulses and reaches ν_{ee}^{*ped} and ρ_i^{*ped} much closer to those expected in ITER.

The variations in T_e^{ped} and n_e^{ped} in the q_{95} scan dataset are not due to a significant variation in the pedestal width and no clear correlation between width and q_{95} is observed. The variation is due to a change in the pedestal gradients, as presented in figure 5 where the maximum pressure gradients in the pedestal versus B_t are shown. Only a minor weak increase in the maximum pressure gradient is observed, figure 5(*a*). This is consistent with the fact that pressure is approximately constant. Instead, the maximum temperature gradient increases with increasing q_{95}, consistent with the increase in T_e^{ped} and the maximum density gradient decreases with increasing q_{95}, consistent with the decreasing n_e^{ped}. The major role of the pedestal gradients has been highlighted also in several other scenarios and machines, as discussed for example in [76].

3.4. Pedestal stability in the q_{95} scan dataset

The stability analysis has been performed for several pulses in the q_{95} scan dataset. The peeling-ballooning stability analysis for pulse #103055, performed at $B_t = 1.7$T and $q_{95} \approx 4.0$, is shown in figure 6(*a*). The x -axis is the normalized pressure gradient α and the y -axis is the maximum flux surface averaged toroidal current density $\langle j_{edge}\rangle_{max}$ in the pedestal region normalized to the average current density j. Within the error bars, the experimental point (grey star) is near the ballooning boundary and limited by high-n ballooning modes, with $n \approx 30-50$. The corresponding radial profile of the eigenfunction for the $n = 20$ mode shows a wide ballooning structure coupled to a narrow edge localized peeling instability, figure 6(*b*). The peeling-ballooning stability analysis for pulse #102752 at $B_t = 3.8$T and $q_{95} \approx 8.5$ is shown in figure 6(*c*). In this case, the experimental point is at the peeling boundary, rather close to the corner of the stability diagram, and limited by low-n modes, with $n = 1$. The corresponding radial profile of the eigenfunction shows a clear peak near the separatrix, highlighting the peeling nature, figure 6(*d*). The peeling characteristic of the mode having the largest amplitude near the X-point can be seen also in the contour plot of the corresponding radial displacement structure, as shown in appendix C (figure 34). Note that the stability diagram for the low ν^* /peeling limited pulse #102752 shown in figure 6(*c*) is qualitatively very similar to the stability diagram of the predicted ITER baseline plasma scenario discussed in [7].

A comparison of the stability diagrams for several pulses at different q_{95} is shown in figure 6(*e*). The increase in q_{95} is correlated with an increase in the experimental normalized pressure gradient and with an increase in the normalized bootstrap current. Also the shape of the stability boundary is affected by the increasing q_{95} with the ballooning side that moves to higher α and the peeling side to higher $\langle j_{edge}\rangle_{max}/j$. The experimental point (the stars) moves upwards with increasing q_{95}, from the ballooning side to the corner of the boundary and finally to the peeling side.

To have a more comprehensive overview of the stability for the entire q_{95} scan dataset, the 1D self-consistent stability analysis has been performed [34]. The results are summarized in

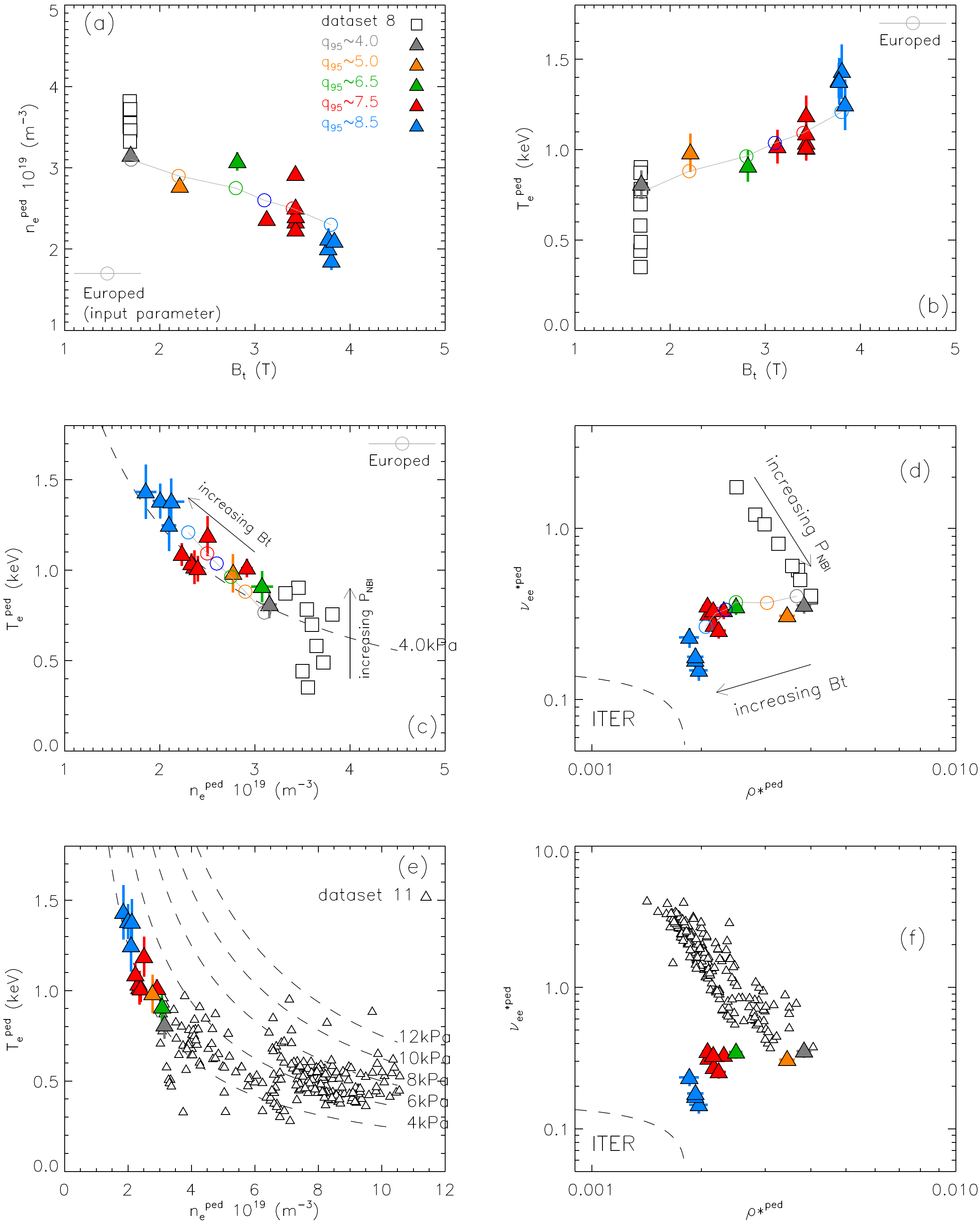

Figure 4. Correlation between electron pedestal density (*a*) and electron pedestal temperature (*b*) with the toroidal field for the q_{95} scan subset at similar gas rate (full triangles) and for the earlier power scan from [69] at $q_{95} = 4.0$ (empty grey triangles, dataset 8). The colors highlight the different B_t and q_{95}. Frame (*c*) shows the correlation between electron pedestal temperature and electron pedestal density. Frame (*d*) shows the correlation between pedestal collisionality and normalized pedestal ion Larmor radius. Frames (*e*) and (*f*) are similar to frame (*d*) and (*e*) but compare the q_{95} scan dataset with all JET-ILW high-δ plasmas until 2020 (dataset 11). The empty circles show the Europed predictions.

figure 6(*f*), where the full triangles show the toroidal harmonic n of the most unstable mode, n_{crit}. Increasing q_{95} leads to a systematic reduction in n_{crit}, from high-n ballooning modes at $q_{95} \approx 4.0$ to low-n peeling modes at $q_{95} \approx 8.5$.

The picture that emerges from figure 6 is that the increase in q_{95} has stabilized the high-n ballooning modes, via the increase of B_t [10, 18], moving the stability boundary to higher α and allowing the pedestal to become limited by low-n

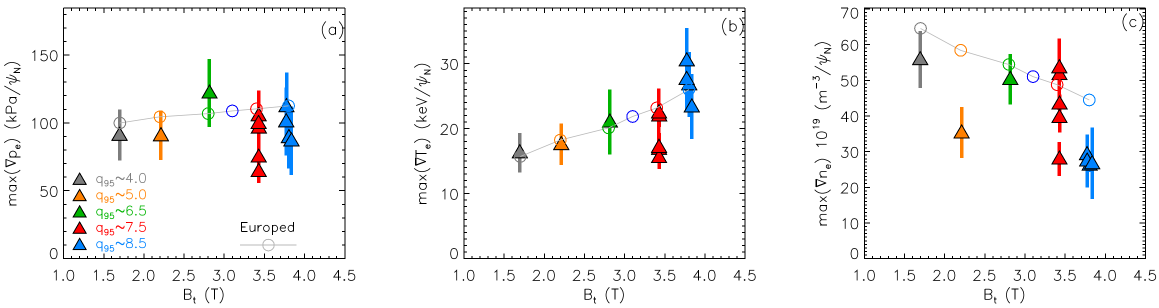

Figure 5. Correlation between maximum pedestal gradients versus toroidal filed for electron pressure (*a*), temperature (*b*) and density (*c*) for the q_{95} scan subsets at similar gas rate. The colors highlight the different B_t and q95. The full triangles show the experimental data and the empty circles the Europed predictions.

peeling modes. By increasing B_t, a higher β_θ can be obtained before reaching the stability limits. In turn, the increased β_θ stabilizes the ballooning modes, which helps to reach peeling limit pedestals.

3.5. Validating the pedestal predictions in the q_{95} scan dataset

The Europed predictions of the pedestal pressure height for a q_{95} scan are shown in figure 7. Input parameters consistent with the pulses of section 3.3 have been used ($I_p = 1.4$MA, high triangularity shape, $\beta_N = 1.7$, $Z_{eff} = 1.5$, zero relative shift and $T_e^{sep} = 200$eV). Two assumptions have been tested for the pedestal density, first assuming constant n_e^{ped}, then assuming n_e^{ped} decreasing with increasing q_{95}, as experimentally reported in figure 4. The two assumptions do not lead to major differences. Two assumptions have been tested also for T_i, first assuming $T_i = T_e$, then assuming a more realistic T_i profile with $T_i^{ped} = 1.2T_e^{ped}$ and $T_i^{sep} = 4T_e^{sep}$ (see appendix A). The two assumptions on T_i lead to qualitatively similar results, but quantitatively the second more realistic assumption produces a higher T_e^{ped} (a sensitivity test on T_i/T_e is discussed in appendix B). Figure 7 shows the predictions only with the realistic assumption on T_i.

The density at the pedestal top, which is an input parameter to the code, is shown in figure 7(*a*), for reference. The predicted pedestal heights are shown in figures 7(*b*) and (*c*) for T_e^{ped} and p_e^{ped} respectively. Both T_e^{ped} and p_e^{ped} increase with increasing q_{95}. The predicted normalized pressure gradients are reported in figure 7(*d*), showing an increasing α_{crit} with increasing B_t. The toroidal mode numbers of the predicted most unstable mode are reported in figure 7(*e*) showing a decreasing n_{crit} with increasing B_t, from high-n modes ($n_{crit} \approx 20-30$) to low-n modes ($n_{crit} \approx 3-4$).

The comparison between experimental data and Europed predictions are shown in previous figures. The predicted T_e^{ped} is compared with the experimental q_{95} scan in figure 4(*b*). Within the experimental uncertainties, the agreement is good. The predicted ν_{ee}^{*ped} and ρ_i^{*ped} are compared with the experimental ones in figure 4(*d*) and the pedestal gradients in figure 5. In both cases the agreement is good. The comparison between the predicted most unstable mode and the pedestal stability analysis is shown in figure 6(*f*). Qualitatively, predictions and stability analysis show similar trends. The minor quantitative disagreement between the experimental data and the Europed modeling are likely due to the fact that only B_t and n_e^{ped} have been changed in the Europed predictions while in the experimental q_{95} scan also other physics parameters, such as β_N, can change from pulse to pulse.

To investigate more in depth the origin for the transition from ballooning to peeling limited plasmas with increasing B_t and q_{95}, figure 8 shows the Europed predicted effect on the $n = 20$ ballooning mode and on the $n = 3$ peeling mode. The increase in q_{95} leads to a clear stabilization of the $n = 20$ ballooning mode, with the critical α that increases from $\alpha_{crit} \approx 5$ at low q_{95} to $\alpha_{crit} > 10$ at high q_{95}. Instead, the increase in q_{95} has only a minor effect on the $n = 3$ peeling mode, figure 8(*b*), and the corresponding α_{crit} remains around 5.5. As shown in figure 8(*c*), at low field ($B_t < 2.8$T) the first mode that become unstable is the $n = 20$. Then, the increasing B_t stabilizes the $n = 20$ mode and at high field ($B_t > 2.8$T) the first unstable mode is the $n = 3$, with the pedestal that becomes limited by low-n peeling modes. Figure 8 shows clearly that the transition from a high-n ballooning limited pedestal at low q_{95} to a low-n peeling limited pedestal at high q_{95} is due to the stabilizing effect of B_t on ballooning modes.

4. Density scans in peeling limited pedestals

This section investigates the effect of the density on peeling limited pedestals and describes experimental pedestal structure, pedestal stability and comparison with pedestal predictions.

Datasets used. Datasets 1–5 have been used. Particular emphasis is given to dataset 5, which is a gas scans at $q_{95} = 8.5$ with constant I_p and input power in deuterium high triangularity plasmas (cyan triangles). Dataset 9 (a gas scan in deuterium high-triangularity plasmas) is used to provide a qualitative comparison with a ballooning limited dataset.

4.1. Deuterium gas rate scans

To obtain a variation in the density, the gas rate has been varied from shot to shot. Plasma current, q_{95}, plasma shape and power have been kept constant. The gas rate

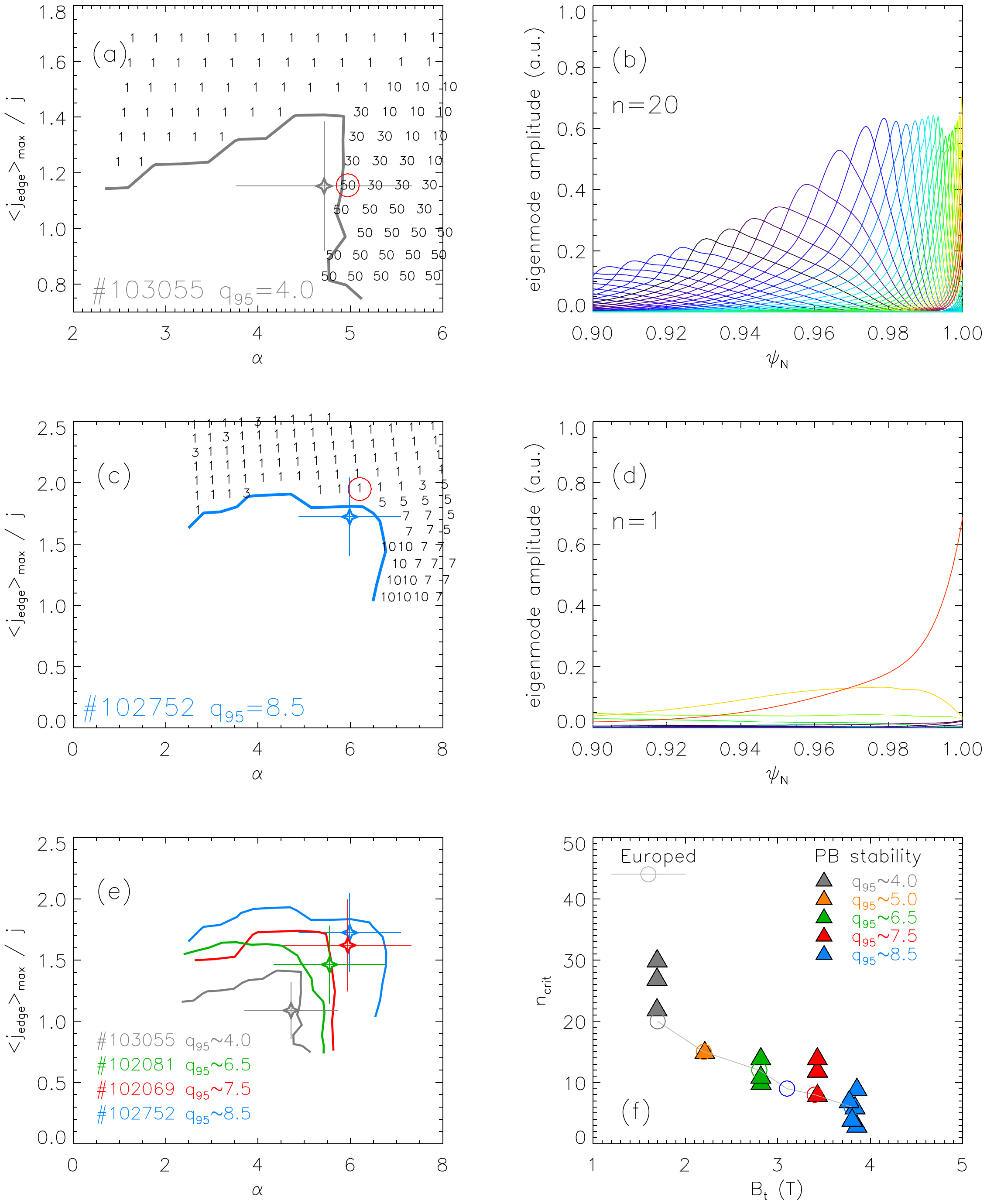

Figure 6. Peeling-ballooning stability analysis for the q_{95} scan subsets at similar gas rate. Frame (*a*) shows the stability analysis for the $B_t = 1.7$ T/$q_{95} = 4.0$ pulse #103481 and frame (*b*) shows the eigenfunction radial profile for the $n = 20$ instability near the experimental point (the red circle in frame a). Frame (*c*) shows the stability analysis for the $B_t = 3.8$ T/$q_{95} = 8.5$ pulse #102752 and frame (*d*) shows the eigenfunction radial profile for the $n = 1$ instability near the experimental point (the red circle in frame c). The stars in frames (*a*) and (*c*) highlight the experimental point, the continuous lines show the stability boundary and the numbers correspond to the most unstable toroidal mode. Frame (*e*) compares the stability boundaries and the experimental points in four pulses at different q_{95}. Frame (*f*) shows with full triangles the most unstable mode versus B_t [34]. The empty circles in frame (*f*) show the pedestal predictions with Europed.

has been changed by one order of magnitude, in the range $\Gamma_D = 0.05 - 1.0 \times 10^{22}\,(\mathrm{e\,s^{-1}})$. The gas scan has been performed mainly at $B_t = 3.8$T /$q_{95} = 8.5$ and at $B_t = 3.4$T /$q_{95} = 7.5$, corresponding to dataset 5 and dataset 4 in table 1, in which peeling limited pedestals have been reached.

The increasing gas rate has led to a decreasing pedestal density. This is shown in figure 9(*a*) where it is particularly clear in the $B_t = 3.8$T /$q_{95} = 8.5$ subset. Initially, the increase of the gas rate does not have a significant effect on n_e^{ped} but for gas rates $\Gamma_D > 0.3 \times 10^{22}\,(\mathrm{e\,s^{-1}})$ the density decreases

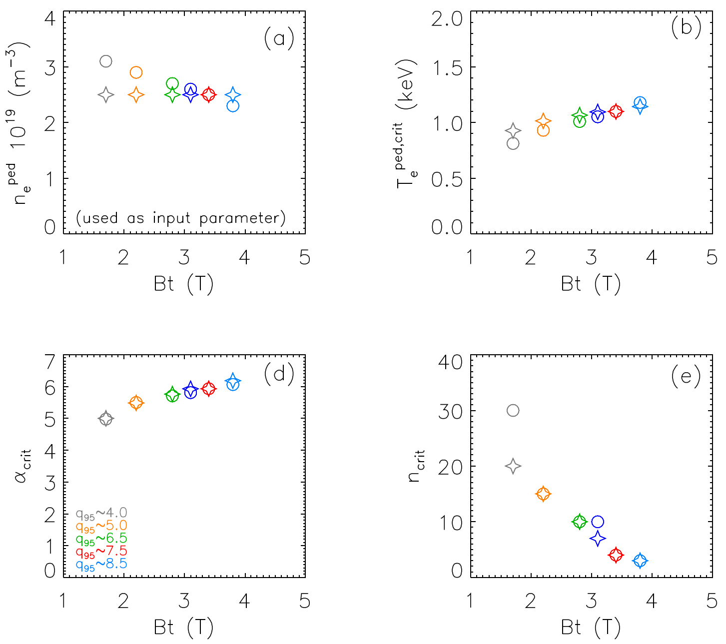

Figure 7. Europed pedestal prediction for a q_{95} scan via the B_t increase at $I_p = 1.4$ MA, $\beta_N = 1.7$, $Z_{eff} = 1.5$, $T_e{}^{sep} = 200$ eV, high-δ, zero relative shift, $T_i{}^{ped} = 1.2 T_e{}^{ped}$ and $T_i{}^{sep} = 4.0 T_e{}^{sep}$. Frame (*a*) shows the input density (constant $n_e{}^{ped}$ with stars and decreasing $n_e{}^{ped}$ with circles). Frame (*b*) and frame (*c*) show the predicted pedestal height for temperature and pressure. Frame (*d*) and frame (*e*) show the corresponding critical normalized pressure gradient and the toroidal number of the most unstable mode.

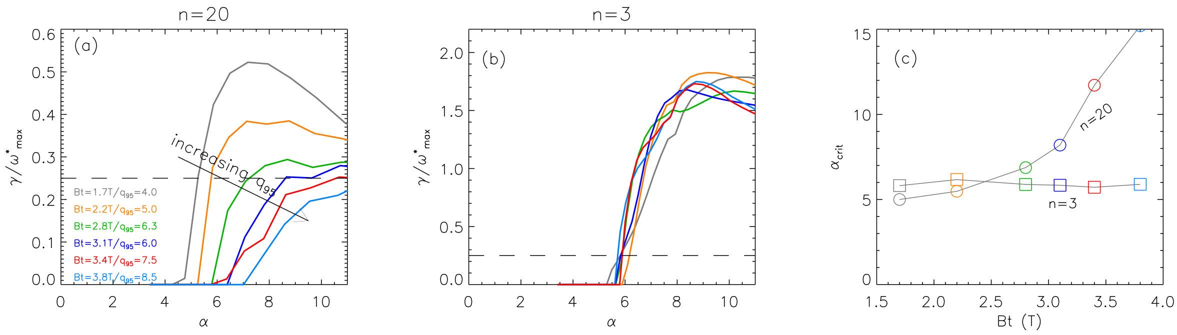

Figure 8. Growth rate of the $n = 20$ ballooning mode (*a*) and $n = 3$ peeling mode (*b*) versus the normalized pressure gradient for different values of the toroidal field at 1.4 MA, $\beta_N = 1.7$, $n_e{}^{ped} = 2.5 \times 10^{19} m^{-3}$, $Z_{eff} = 1.5$, $T_e{}^{sep} = 200$ eV, high-δ. The dashed line in frames (*a*) and (*b*) highlights the critical threshold above which the mode is considered unstable. Frame (*c*) shows the corresponding critical α versus the toroidal field.

from $2.5 \times 10^{19}\ (m^{-3})$ to $2.0 \times 10^{19}\ (m^{-3})$. The correlation is opposite at the separatrix, where an increase of n_e^{sep} with increasing gas rate can be seen, figure 9(*b*). While the positive correlation between n_e^{sep} and gas rate is reasonable, the negative correlation between n_e^{ped} and gas rate is counterintuitive. This negative trend might be ascribed to the increased ELM particle losses. The increasing gas rate leads to an increasing f_{ELM} which, in turn, is correlated to a decrease in n_e^{ped}, figures 9(*c*) and (*d*). The increase in f_{ELM} likely leads to an increase in ELM particle losses as discussed in [65]. Moreover, the negative correlation might be amplified by an increased SOL opacity (due to the increased n_e^{sep}), not allowing the neutrals to be ionized inside the separatrix [77, 78]). The behavior of T_i with the gas rate is discussed in appendix A.

4.2. Effects of pedestal top density on the pedestal structure and pedestal stability

The profiles of two pulses from dataset 5 (with $q_{95} = 8.5$, $P_{aux} = 25$MW and high triangularity) at low pedestal density and high pedestal density are shown in figure 10. The pre-ELM profiles of electron temperature, electron density and ion temperature are shown respectively in figures 10(*a*)–(*c*). The increase in the density is correlated to a negligible reduction in T_e^{ped} and to a weak increase in T_i^{ped}, therefore producing an increase in the pedestal top pressure, as later discussed.

The pedestal stability for the low and the high n_e^{ped} pulses is shown in figures 11(*a*) and (*c*) respectively. In the low density pulse, the toroidal number of the most unstable mode is $n = 1$. The radial profiles of the corresponding eigenfunction

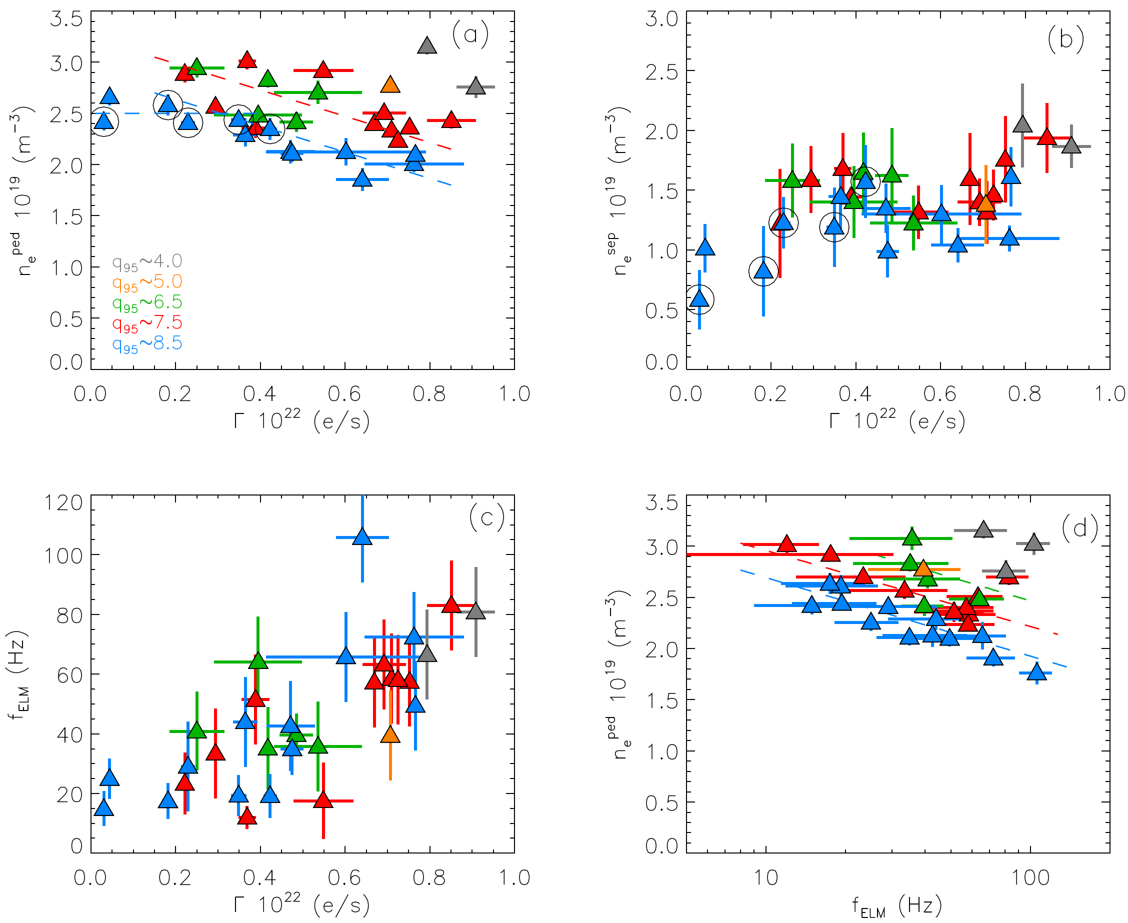

Figure 9. Correlation of $n_e{}^{ped}$ (*a*), $n_e{}^{sep}$ (*b*) and f_{elm} (*c*) with gas rate. Correlation between $n_e{}^{ped}$ and f_{ELM} (*d*). The dataset is characterized by $I_p = 1.4$ MA, high-δ, $P_{aux} = 25$ MW. The colors highlight the different B_t and q_{95}. The empty circles in frames (*a*) and (*b*) highlight the $n_e{}^{sep}/n_e{}^{ped}$ scan discussed in section 5.

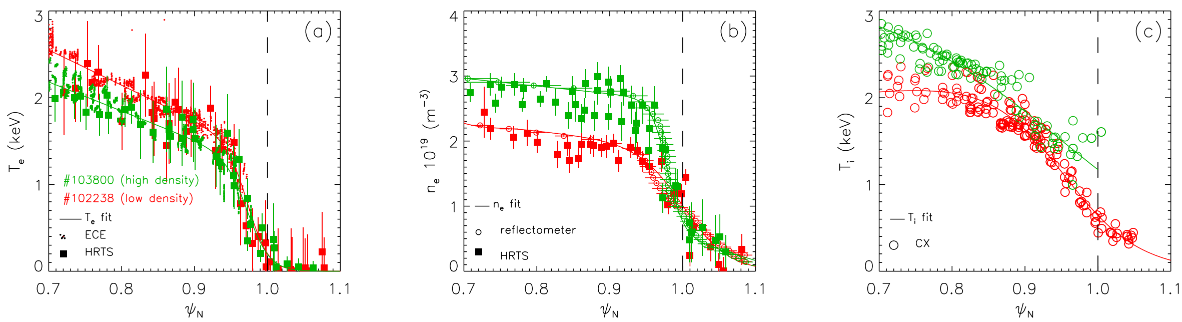

Figure 10. Pre-ELM profiles of electron temperature (*a*), electron density (*b*) and ion temperature (*c*) of a low density pulse (red) and a high density pulse (green) at $q_{95} = 8.5$.

are reported in figure 11(*b*), showing a clear peeling characteristic, with the perturbation localized at the edge (the 2D structure of the radial displacement is shown appendix C, figure 35). In the high density pulse, the toroidal number is around $n \approx 3-5$. In this case, the eigenfunction shows a peeling component localized at the edge that is coupled to smaller amplitude ballooning components. This highlights that the increase of the density can move the pedestal from being peeling limited towards being peeling-ballooning limited.

The correlation between the pedestal height of temperature and pressure versus the pedestal density is presented in figure 12 for the entire dataset 5 ($q_{95} = 8.5$, $P_{aux} = 25$MW and high triangularity). The increase of n_e^{ped} at constant q_{95} does not affect significantly the pedestal electron temperature. Due to the fact that T_e^{ped} is not significantly affected, the pedestal electron pressure increases with increasing density. Similar behaviors have been observed also for the pedestal ion temperature and the pedestal total pressure, as shown in appendix A.

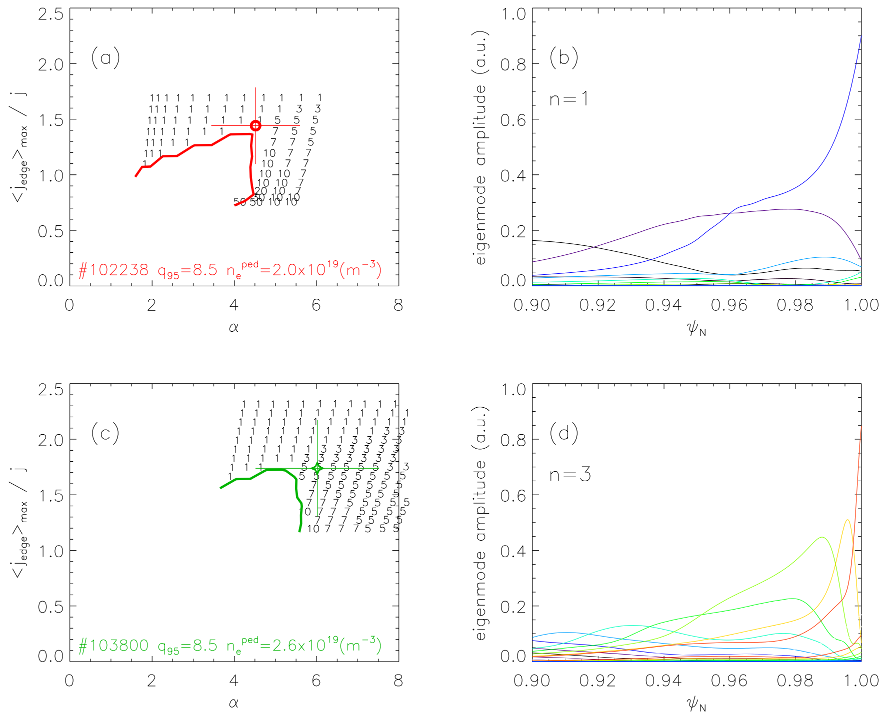

Figure 11. Pedestal stability for (*a*) the low density pulse and (*b*) corresponding radial profile of the $n = 1$ eigenfunction. Pedestal stability for (*c*) the high density pulse and (*b*) corresponding radial profile of the $n = 3$ eigenfunction. The continuous lines in the stability diagrams highlight the stability boundary and the star highlights the experimental point. The numbers identify the most unstable mode. The eigenfunctions are calculated for α and j close to the experimental point.

Note that the correlation shown in figure 12 between pedestal pressure and pedestal density is different from what is observed in ballooning limited pedestals both in JET [70] and in other machines [3, 23, 41], where no correlations or negative correlations were observed. Therefore, the positive correlation of figure 12(*b*) can be considered another signature that peeling limited pedestals have been reached [10].

Note that figure 12(*b*) shows an increase in the pedestal pressure with increasing q_{95} at constant density (we remind that the increasing q_{95} is obtained via the B_t increase). This trend is different from the result of figure 4(*a*), where p_e^{ped} was approximately constant. The contradiction is explained by the fact that the data of figure 4 were characterized by a decreasing n_e^{ped} with increasing q_{95}. Indeed, the experimental increase of the p_e^{ped} with increasing q_{95} at constant n_e^{ped} is consistent with the Europed modeling of the earlier figure 7(*c*).

The increase of the pedestal pressure with increasing n_e^{ped} is due to the increase in the pedestal gradients while no clear correlation has been observed between pedestal width and n_e^{ped}, within the scatter of the data. The correlations between the maximum pedestal gradients and n_e^{ped} are shown in figure 13. Figure 13(*a*) provides two important information:

- at constant q_{95}, a clear increase of ∇p_e with increasing n_e^{ped} can be observed. This behavior is opposite to that observed in ballooning limited pedestals [70].
- At constant n_e^{ped} the increase in q_{95} leads to the increase in ∇p_e. This experimental result is consistent with the Europed modeling discussed in figure 7(*d*).

Figures 13(*b*) and (*c*) provide two important information:

- while no correlation between ∇T_e and n_e^{ped} is present at constant q_{95}, a clear correlation between ∇n_e and n_e^{ped} can be seen. So, the positive correlation between ∇p_e and n_e^{ped} is not due to an effect of the temperature, but to an effect of the density.
- ∇T_e increases with increasing q_{95} at roughly constant n_e^{ped}. So, the increase in ∇p_e with increasing q_{95} is due to an effect of the temperature.

Therefore, the increase of the pedestal pressure with increasing pedestal density in the peeling limited plasmas might be due to two mechanisms. First of all, the increase of ∇p_e with increasing n_e^{ped} suggests an improvement in the pedestal stability with increasing n_e^{ped}. Indeed, this can be seen in the stability diagram of figure 11. This mechanism is tested in the next section with the Europed modeling. Furthermore, the increase of ∇n_e with increasing n_e^{ped} suggests also a reduction in the particle transport. Unfortunately, this second process cannot be experimentally confirmed due to the lack of measurement of particle sources in JET.

To have a comprehensive overview of the behavior of the pedestal structure in peeling limited pedestals, figure 14 shows data for pedestal width, pedestal position and n_e^{sep}/n_e^{ped}. The pedestal width is shown in figure 14(*a*) versus the poloidal beta at the pedestal top. The dashed line shows the EPED1 assumption discussed in expression (4) [4]. The dataset discussed in this work (the full triangles) does not show any clear correlation with β_θ^{ped}. However, by including all previous JET-ILW

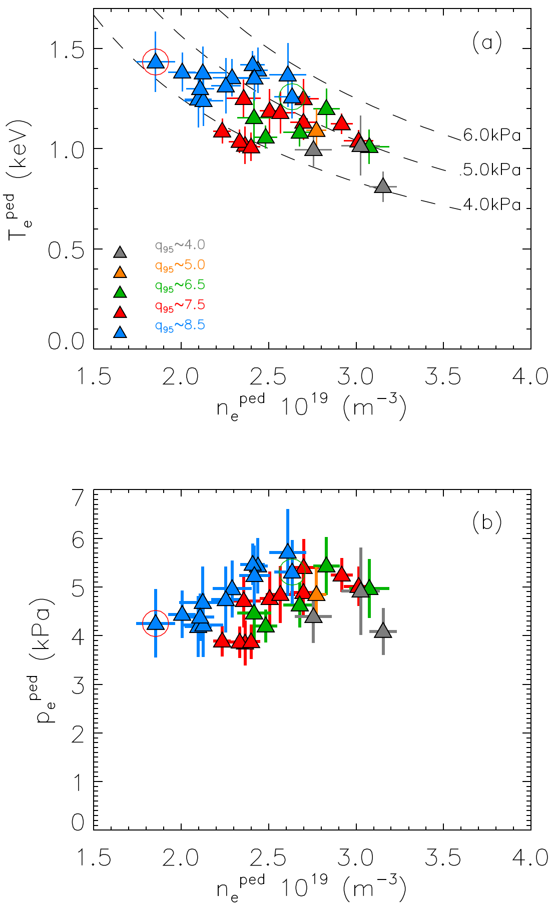

Figure 12. Correlation between pedestal height of electron temperature (*a*) and electron pressure (*b*) versus the electron pedestal density. The colors highlight the different B_t and q_{95}. The green and red circles highlight the pulses shown in figures 10 and 11.

high-δ plasmas (dataset 11), a reasonable agreement with the EPED1 assumption can be seen. No trend between the pedestal width and q_{95} can be seen, as mentioned earlier. The ratio n_e^{sep}/n_e^{ped} is shown in figure 14(*b*). n_e^{sep}/n_e^{ped} increases from ≈ 0.3 at low gas rate to ≈ 0.7 at high gas rate. Finally, the correlation between the position of the pedestal density and n_e^{sep}/n_e^{ped} is shown in figure 14(*c*). The correlation for the main dataset (full triangles) is consistent with earlier trends in ballooning limited dataset (dataset 11).

4.3. Pedestal predictions of n_e^{ped} effects in peeling limited plasmas and comparison with ballooning limited pedestals

The Europed modeling has used as reference the lowest n_e^{ped} plasma of the $q_{95} = 8.5$ density scan (corresponding to the input parameters $n_e^{ped} = 1.8 \times 10^{19}\,(\mathrm{m}^{-3})$, $\beta_N = 1.7$, $Z_{eff} = 1.5$, zero relative shift, $T_e^{sep} = 200\mathrm{eV}$, $T_i^{ped} = 1.2T_e^{ped}$ and $T_i^{sep} = 4T_e^{sep}$). The modeling has been repeat by increasing n_e^{ped} while keeping constant all other input parameters. The predictions are shown in figure 15(*a*), where the Europed results (empty grey symbols) are compared with the experimental data (full triangles). The Europed predictions show a clear positive correlation between p_e^{ped} and n_e^{ped}, in qualitative agreement with the experimental results. Quantitatively, the increase of p_e^{ped} with increasing n_e^{ped} is weaker than the experimental results. A possible reason is that in the Europed modeling only n_e^{ped} is changed, while experimentally the high density pulses have also slightly different β_N, relative shift, and T_i/T_e. In particular, the high density pulse has $\beta_N = 2.1$ which is significantly higher than in the low density pulse ($\beta_N = 1.7$). Indeed, repeating the Europed modeling at higher β_N brings the predictions closer to the experimental results, as shown by the empty grey diamond in figure 15(*a*).

The predicted gradients are compared with the experimental gradients in the earlier figure 13. From a qualitative point of view, the predictions are in reasonable agreement with the experimental trends. Both the predictions and the experimental results show a positive correlation between ∇p_e and n_e^{ped}, and between ∇n_e and n_e^{ped}.

Europed predicts that the pedestal remains limited by instabilities characterized by low n also at the highest density reached. In figure 15(*b*), the critical n predicted by Europed is shown versus n_e^{ped}. Within the density range investigated, $n_{crit} = 2$ at $\beta_N = 1.7$, while n_{crit} increases from 2 to 7 at $\beta_N = 2.1$. These values are consistent with those obtained by the peeling-ballooning stability analysis of figure 11 using the experimental profiles.

Figure 15(*c*) shows the pre-ELM pressure profiles for the low density pulse and the high density pulse. The experimental results are compared with the critical profiles from Europed. A good qualitative agreement can be seen, while quantitatively the predictions slightly underestimate the experimental results. The disagreement is due to a predicted pedestal width that is narrower than the experimental one. This issue is common in JET-ILW and has been discussed in earlier works [42, 79].

The pedestal predictions in peeling limited plasmas are compared with pedestal predictions in ballooning limited plasmas in the right column of figure 15. The experimental dataset 9 is used. The pedestal pressure slightly decreases with increasing density. Experimentally, this is due to a strong reduction in the pressure gradient which is partially compensated by a widening of the pedestal [70]. The Europed predicted pedestal pressure shows a weak decrease with increasing n_e^{ped}, in agreement with the experimental results. The most unstable mode is in the range $n_{crit} = 40 - 50$, so the predicted pedestal is clearly limited by ballooning modes, as shown in figure 15(*e*). The comparison pre-ELM profiles versus predicted critical profiles is shown in figure 15(*f*). A qualitative agreement can be seen.

The link between density and pedestal stability is investigated with Europed in figure 16. Figure 16(*a*) shows the predicted growth rate of a $n = 2$ peeling mode versus the normalized pressure gradient. The destabilization of the mode occurs at higher α as the density increases, showing that the increasing density has a stabilizing effect on the $n = 2$ mode. Indeed, the corresponding α_{crit} increases with increasing density, as shown in figure 16(*b*). A similar analysis is done for the $n = 50$ ballooning mode in figure 16(*c*). In this case, the increasing density has a destabilizing effect and the corresponding α_{crit} decreases with increasing n_e^{ped}.

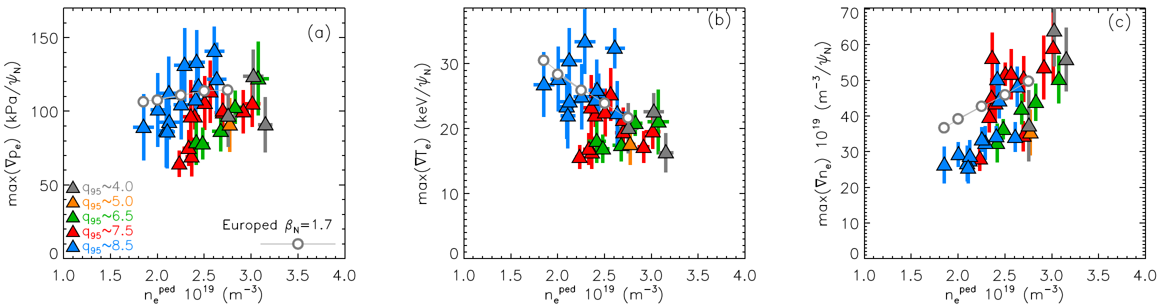

Figure 13. Correlation between the maximum pedestal pressure gradient of electron pressure (*a*), temperature (*b*) and density (*c*) versus the pedestal density. The colors highlight the different B_t and q_{95}. The empty circles highlight the Europed predictions at $\beta_N = 1.7$ for the dataset at $B_t/q_{95} = 3.8$ T/8.5.

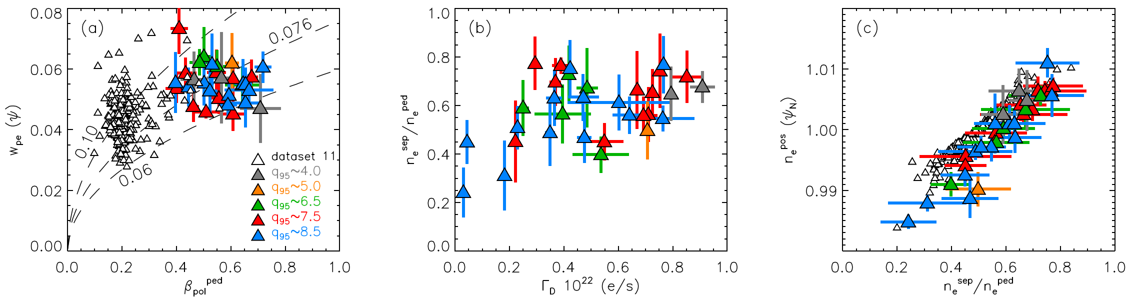

Figure 14. Correlation between pressure pedestal width and beta poloidal at the pedestal (*a*), between n_e^{sep}/n_e^{ped} and gas rate (*b*) and between position of electron pedestal density and n_e^{sep}/n_e^{ped} (*c*). The colors highlight the different B_t and q_{95}. The full symbols identify the new dataset used in this work and the empty symbols represents all the earlier high-δ H-modes in JET-ILW until 2020.

The analysis done in figure 16 shows that the increase in pedestal pressure with increasing n_e^{ped} is due to the stabilizing effect of the density on peeling modes. The increasing density increases the collisionality which in turn reduces the bootstrap current and hence increases the shear. The reduced bootstrap current and the increased shear have a stabilizing effect on the peeling mode.

5. Effect of separatrix density in peeling limited pedestals

Investigation of peeling limited pedestals at high n_e^{sep}/n_e^{ped} and low collisionality is very important as ITER is supposed to operate at $n_e^{sep}/n_e^{ped} > 0.6$ [43]. The datasets discussed in this work is very useful for this investigation as it has been able to reach high n_e^{sep}/n_e^{ped} while remaining at low collisionality. As shown in figure 17, no earlier high triangularity JET-ILW datasets have reached this range of parameters and have approached the ITER-relevant range.

Datasets used. A subset of dataset 5 at constant n_e^{ped} has been used ($B_t = 3.8$T $/q_{95} = 8.5$ with constant I_p, and input power in deuterium high triangularity plasmas). Since n_e^{ped} affects the pedestal, the subset has been selected with approximately constant density, $n_e^{ped} = 2.6 \times 10^{19}$ (m^{-3}). This subset is highlighted by empty circles in figures 9 and 17. Dataset 10 (a n_e^{sep}/n_e^{ped} scan in deuterium low-triangularity plasmas) is used to provide a qualitative comparison with ballooning limited plasmas.

5.1. Effects of n_e^{sep}/n_e^{ped} on the pedestal structure and pedestal stability

The pre-ELM profiles of two pulses with low and high n_e^{sep}/n_e^{ped} at $B_t = 3.8$T $/q_{95} = 8.5$ and $n_e^{ped} = 2.6 \times 10^{19}$ (m^{-3}) are shown in figure 18. Despite the different n_e^{sep}/n_e^{ped}, the electron temperature and ion temperature at the pedestal top are very similar. The pedestal pressure profile is shifted more radially outwards in the high n_e^{sep}/n_e^{ped} pulse, but the pedestal pressure heights are comparable.

The negligible effect of n_e^{sep}/n_e^{ped} on the pedestal height is confirmed in figure 19 by investigating the entire subset. The pedestal heights of electron pressure and temperature are shown in figures 19(*a*) and (*b*) respectively and no clear correlation with n_e^{sep}/n_e^{ped} can be seen. The ion temperature and the total pressure have a similar behavior, as shown in appendix A (figure 33). These behaviors are very different from those in ballooning limited pedestals, where the pedestal pressure shows a clear reduction with increasing n_e^{sep}/n_e^{ped} [24–26, 40].

The detailed behavior of the pedestal structure is partially unexpected. While no clear correlation between pedestal width and n_e^{sep}/n_e^{ped} has been observed (not shown here), the pedestal gradients are correlated with n_e^{sep}/n_e^{ped}. The electron pressure gradient is characterized by a weak decrease with increasing n_e^{sep}/n_e^{ped}, as shown in figure 20(*a*). This decrease is not due to a change in the electron temperature gradient, as shown in figure 20(*b*) but by a weak reduction in the density gradient, as shown in figure 20(*c*). The reduction in the pressure

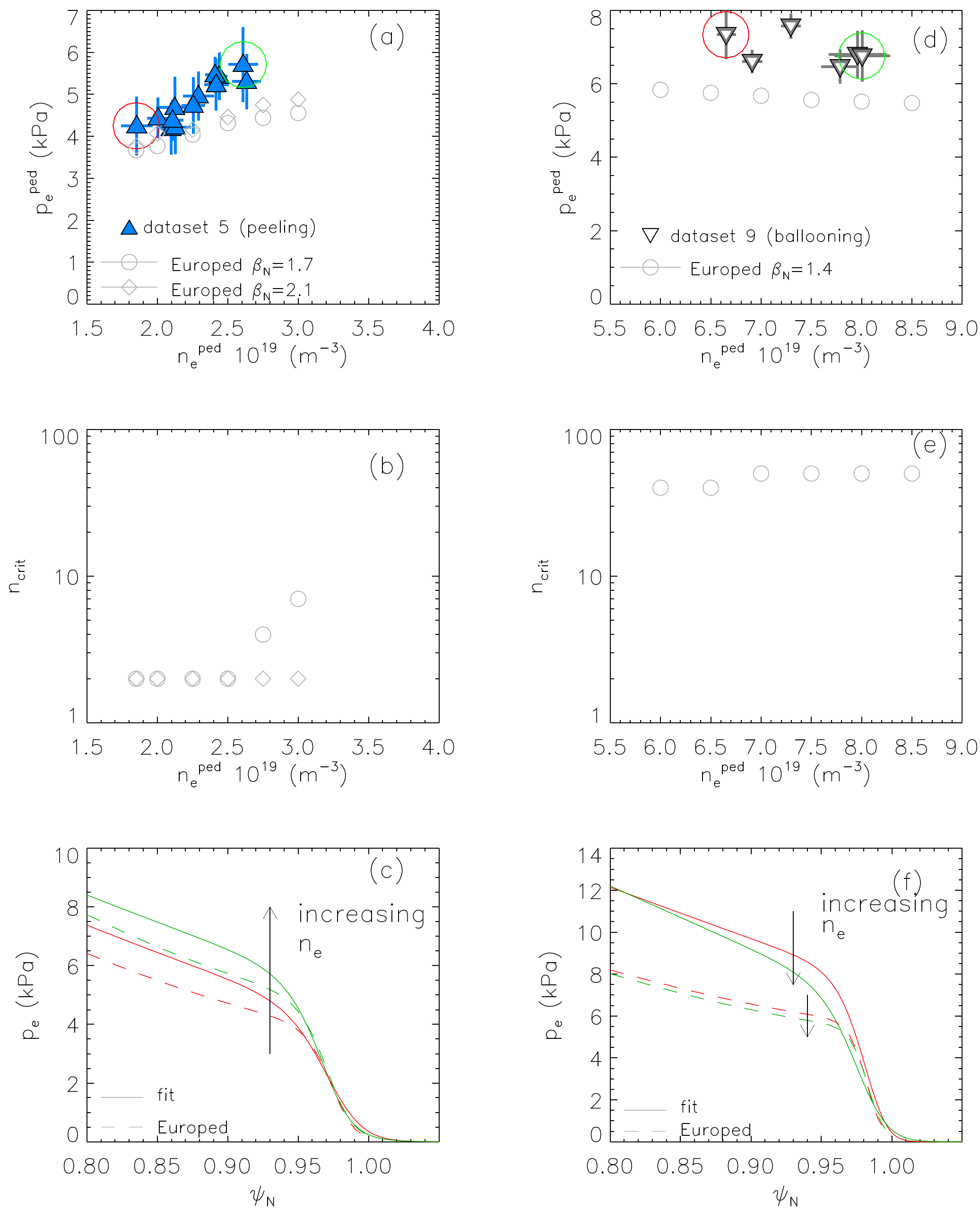

Figure 15. Correlation between $p_e{}^{ped}$ and $n_e{}^{ped}$ for the (*a*) peeling limited dataset at $q_{95} = 8.5$ and (*d*) the ballooning limited dataset 8 [70]. The triangles show the experimental data and the grey empty circles the Europed predictions. Frames (*b*) and (*e*) show the corresponding critical *n*. The pressure profiles (determined from the T_e fit and the n_e fit of figure 10) are shown as continuous lines in frame (*c*) and (*f*), while the Europed predicted profiles are shown as dashed lines. The profiles correspond to the data highlighted with circles in frame (*a*) and frame (*d*).

gradient suggests a reduction of the pedestal MHD stability with increasing n_e^{sep}/n_e^{ped}. So, despite the decreasing pressure gradient with increasing n_e^{sep}/n_e^{ped} and the pedestal width is not being affected, the pedestal pressure at the pedestal top remains constant. This is because the weak reduction in the pressure gradient is compensated by the increase in the separatrix pressure (due to the n_e^{sep} increase), as shown in figure 19(*c*).

The pedestal stability for the lowest and highest n_e^{sep}/n_e^{ped} pulses is shown in figure 21. The low n_e^{sep}/n_e^{ped} pulse is located near the stability boundary with the most unstable modes in the range $n \approx 3-5$. The corresponding eigenfunctions are similar to those shown in figure 11(*b*), with a clear peeling mode localized at the plasma edge. The high n_e^{sep}/n_e^{ped} pulse is located in a region with slightly higher modes, with $n \approx 5-10$. The corresponding eigenfunctions have a peeling component clearly coupled to radially wider ballooning modes. This suggests that the increase in n_e^{sep}/n_e^{ped} can affect the type of pedestal instability and can lead to a transition from peeling limited pedestals to coupled peeling-ballooning limited pedestals.

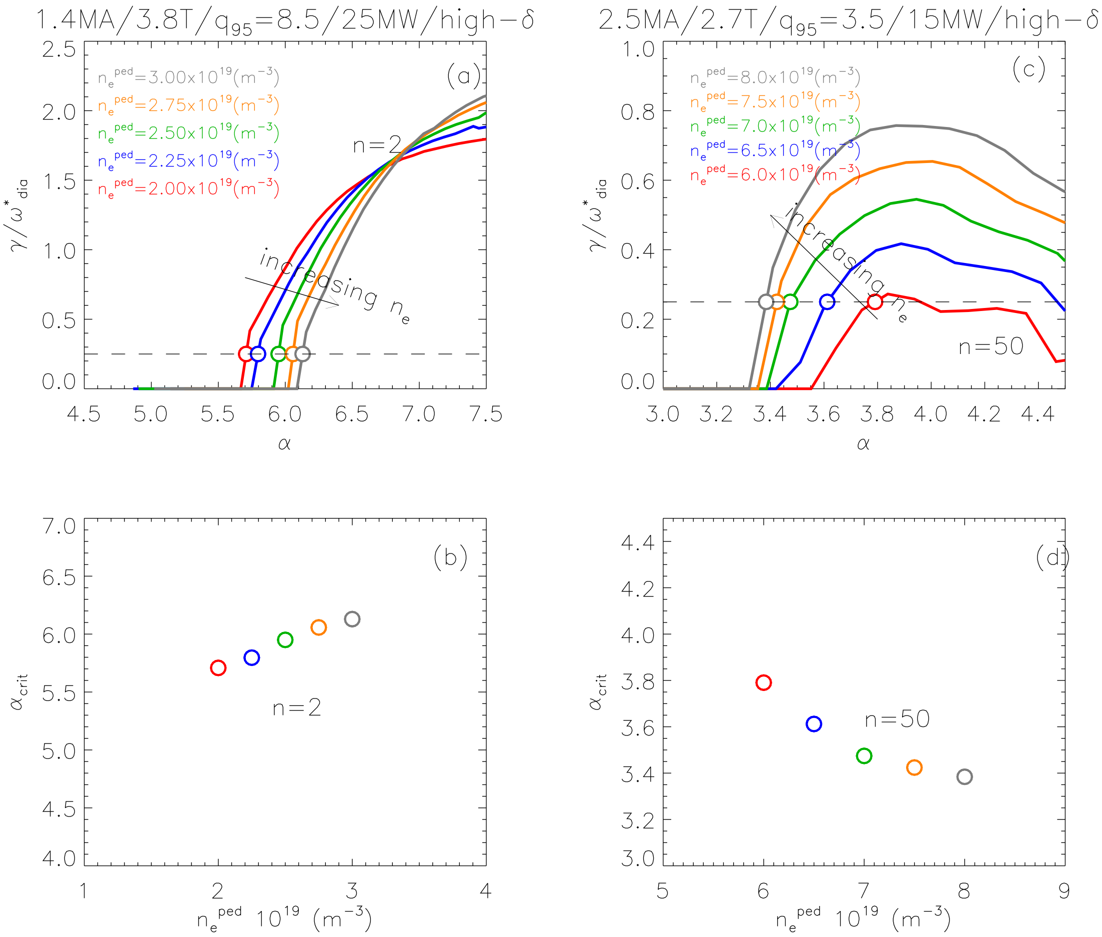

Figure 16. (*a*) Growth rates versus normalized pressure gradient of the $n = 2$ peeling mode for the Europed modeling of figure 15(*a*). Frame (*b*) shows the corresponding critical pressure gradient versus the pedestal density. Frame (*c*) and frame (*d*) show a similar analysis of the $n = 50$ ballooning mode for the Europed modeling of figure 15(*d*).

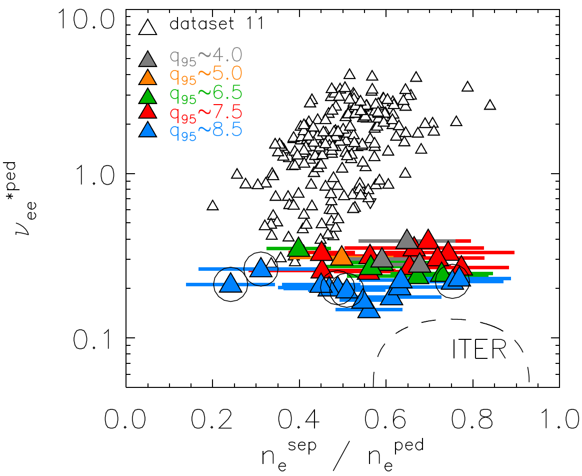

Figure 17. Ranges of pedestal collisionality and n_e^{sep}/n_e^{ped} achieved for the main dataset (full triangles) and the earlier high-δ JET-ILW pulses (dataset 11). The empty circles highlight the subset of the main dataset used in section 5.

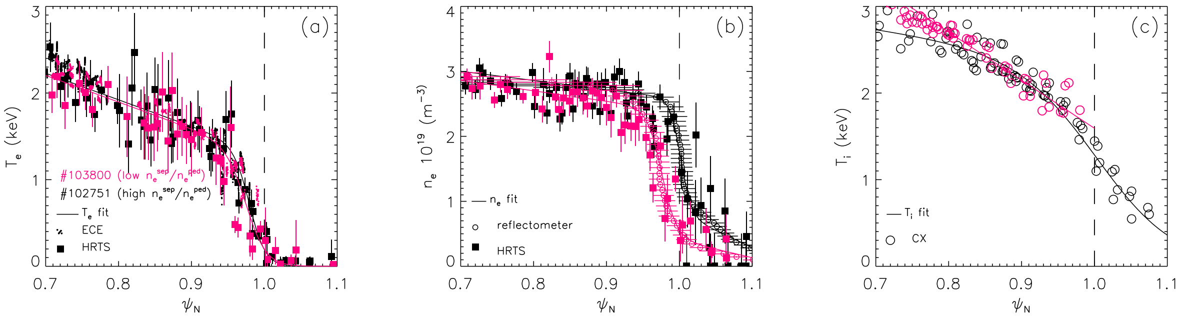

Figure 18. Comparison of the pre-ELM profiles of electron temperature (*a*), electron density (*b*) and ion temperature (*c*) for a low $n_e{}^{sep}/n_e{}^{ped}$ pulse (pink) and a high $n_e{}^{sep}/n_e{}^{ped}$ (black) at 1.4 MA/3.8 T, $q_{95} = 8.5$ and $n_e{}^{ped} = 2.6 \times 10^{19}(\mathrm{m}^{-3})$. The symbols highlight the experimental pre-ELM profiles and the continuous lines the corresponding fits.

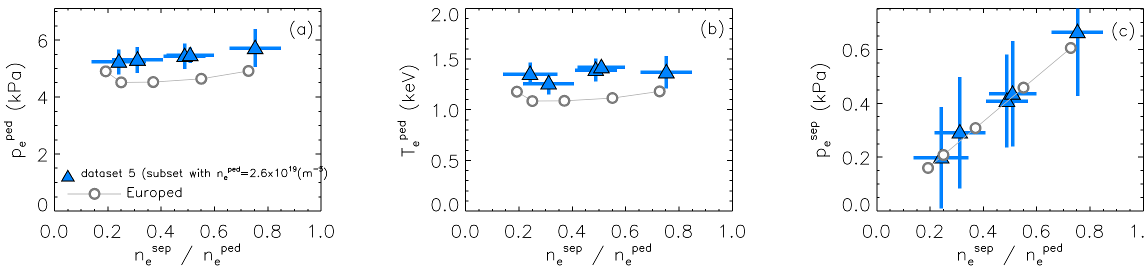

Figure 19. Pedestal height of electron pressure (*a*) and temperature (*b*) versus the ratio $n_e{}^{sep}/n_e{}^{ped}$ for the subset at 1.4 MA/3.8 T, $q_{95} = 8.5$ and $n_e{}^{ped} = 2.6 \times 10^{19}(\mathrm{m}^{-3})$. Frame (*c*) shows electron pressure evaluated at the separatrix. The triangles highlight the experimental data while empty circles the Europed predictions.

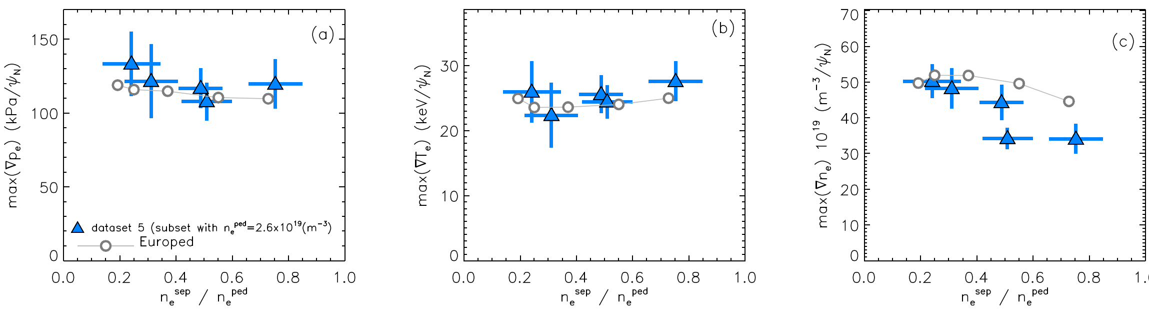

Figure 20. Pedestal gradients of electron pressure (*a*), temperature (*b*) and density (*c*) versus the ratio $n_e{}^{sep}/n_e{}^{ped}$ for the subset at 1.4 MA/3.8 T, $q_{95} = 8.5$ and $n_e{}^{ped} = 2.6 \times 10^{19}(\mathrm{m}^{-3})$. The triangles highlight the experimental data while empty circles the Europed predictions.

5.2. Pedestal predictions of n_e^{sep}/n_e^{ped} effects in peeling limited plasmas and comparison with ballooning limited pedestals

Europed has been used to predict the effect of n_e^{sep}/n_e^{ped}. First, Europed has been applied to the reference plasma #103800, corresponding to the low n_e^{sep}/n_e^{ped} pulse of figure 18 (input parameters $I_p = 1.4MA$, $B_t = 3.8T$ (corresponding to $q_{95} = 8.5$), $n_e^{ped} = 2.6 \times 10^{19}\left(\mathrm{m}^{-3}\right)$, $\beta_N = 1.7$, $Z_{eff} = 1.5$, $T_e^{sep} = 200\mathrm{eV}$, $T_i^{ped} = 1.2T_e^{ped}$, $T_i^{sep} = 4T_e^{sep}$ and $n_e^{sep}/n_e^{ped} = 0.25$). Then, the simulation has been repeated by changing the relative shift while keeping all other input parameters constant. The predicted pedestal pressure is compared to the experimental p_e^{ped} in figure 22(*a*). A good qualitative agreement between predictions and experimental data can be observed. In particular, the pedestal predictions do not show any strong pedestal degradation with increasing n_e^{sep}/n_e^{ped}. A more detailed comparison between pedestal predictions and experimental data is shown in the earlier figures 19 and 20, where reasonable qualitative agreements can be seen also for the pedestal gradients. Note that the predictions show a non-decreasing p_e^{ped} with increasing n_e^{sep}/n_e^{ped} despite the decreasing ∇p_e. This is due to the fact that the decreasing ∇p_e is partially compensated by the increasing p_e^{sep}, in very good agreement with the experimental results of figure 19(*c*).

The comparison between the experimental and predicted pressure profiles for the low and high n_e^{sep}/n_e^{ped} pulses is shown in figure 22(*c*). Qualitatively, the behavior of the pressure is very well reproduced, both in terms of pedestal height and pedestal positions.

For comparison, the right frames of figure 22 show the behavior in a ballooning limited dataset (dataset 10 from

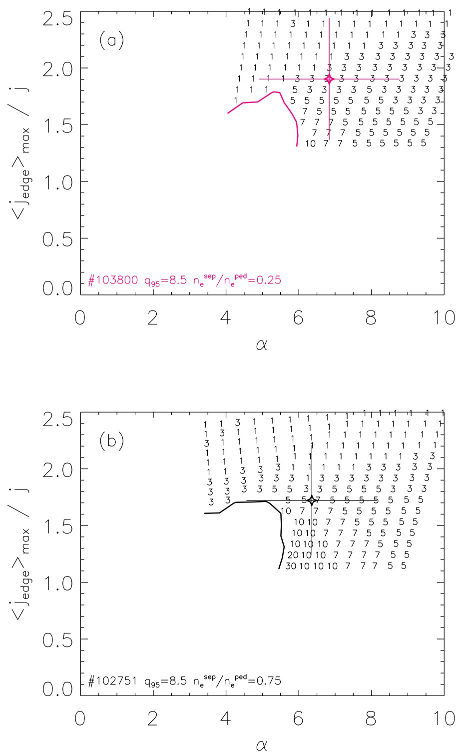

Figure 21. Pedestal stability for low n_e^{sep}/n_e^{ped} pulse (pink), frame (*a*) and the high n_e^{sep}/n_e^{ped} pulse (black), frame (*b*), shown in figure 19. The thick line highlights the stability boundary and the star highlights the operational point. The numbers identify the most unstable mode.

table 1). A clear negative correlation between p_e^{ped} and n_e^{sep}/n_e^{ped} can be seen in the experimental data. The corresponding Europed modeling shows that a clear reduction in the pedestal pressure is followed by a saturation for $n_e^{sep}/n_e^{ped} > 0.5$. The predictions are in agreement with the experimental data only at low n_e^{sep}/n_e^{ped}, as observed in earlier works on ballooning limited pedestals [40].

A difference in the qualitative behavior of the pedestal predictions can be seen between the peeling case and the ballooning case. In the peeling case, a very weak correlation between p_e^{ped} vs n_e^{sep}/n_e^{ped} can be observed, while in the ballooning case a negative correlation is followed by a saturation. This difference is due to the type of predicted instabilities, as shown in figures 22(*b*) and (*e*). In the left frame, the most unstable mode is in the range $n = 2 - 10$. In the right frame, at $n_e^{sep}/n_e^{ped} > 0.3$ the most unstable mode is $n = 30 - 50$, so clearly a ballooning instability. Figures 22(*b*) and (*e*) also suggest that the increase of n_e^{sep}/n_e^{ped} affects the type of the pedestal instability. In figure 22(*e*), a sudden transition from a low-n peeling instability to a high-n ballooning instability can be seen at $n_e^{sep}/n_e^{ped} \approx 0.3$. In figure 22(*b*), the increase of n_e^{sep}/n_e^{ped} leads to an increase in the toroidal number from $n = 2$ to $n = 8 - 10$. This result is important in view of ITER operation. Since ITER is supposed to operate at high n_e^{sep}/n_e^{ped}, its pedestal might not be limited by very low-n instabilities.

For completeness, the behavior of a peeling mode and of a ballooning mode versus n_e^{sep}/n_e^{ped} is discussed in figure 23. A set of Europed simulations has been performed with different n_e^{sep}/n_e^{ped} for the $n = 2$ peeling mode, and the $n = 50$ ballooning mode. For the $n = 2$ mode, no significant effect can be seen on α_{crit}, apart a weak reduction at $n_e^{sep}/n_e^{ped} > 0.45$. The behavior is different for the $n = 50$ mode which shows a strong destabilization at $n_e^{sep}/n_e^{ped} < 0.45$, followed by a saturation.

6. Effect of isotope mass in peeling limited pedestals

To assess the role of the isotope mass in low ν^*/peeling limited plasmas, gas rate scans at $I_p = 1.4$MA, $B_t = 3.8$T (corresponding to $q_{95} = 8.5$), $P_{NBI} = 25$MW and high triangularity have been performed during the DTE3 JET-ILW campaign. A gas scan has been performed in mixed deuterium/tritium (D/T) plasma, with effective mass $A_{eff} = 2.5$ and a gas scan in tritium-rich (T-rich) plasmas, with $A_{eff} = 2.9$. In both datasets, the NBI was operated in deuterium. $A_{eff} = 2.9$ was the highest possible during DTE3 and was achieved by injecting as fuelling gas only tritium while still operating the beams in deuterium.

Datasets used. This section uses datasets 5, 6 and 7, which are gas scans at $q_{95} = 8.5$ with constant I_p and input power in deuterium, mixed deuterium-tritium and tritium-rich high triangularity plasmas. Dataset 12 (isotope mass scan at constant β_N in low-triangularity plasmas) is used to provide a qualitative comparison with a ballooning limited dataset.

6.1. Effects of isotope mass on the pedestal structure and pedestal stability

The effect of the isotope mass on the pedestal profiles of temperature and density is shown in figure 24. The two pulses shown in figure 24 have the same engineering parameters (1.4MA, 3.8T, $q_{95} = 8.5$, $P_{aux} = 25$MW, high triangularity) including the gas rate, 4×10^{21} (es^{-1})), but different isotope mass. Pulse #103705 is in pure deuterium with $A_{eff} = 2.0$ and pulse #104280 is tritium-rich, with $A_{eff} = 2.9$. The $A_{eff} = 2.9$ pulse has higher electron density at the pedestal top than the $A_{eff} = 2.0$ pulse, but similar electron temperature. The ion temperature is slightly higher in the tritium-rich pulse. This behavior is similar to that in ballooning limited plasmas in JET-ILW [66, 80].

To verify if peeling limited pedestals have been achieved also in plasmas with $A_{eff} > 2$, the pedestal stability is investigated in figure 25. The two pulses selected for the stability analysis are the $A_{eff} = 2.5$ pulse with highest density and the $A_{eff} = 2.8$ pulse with highest density. The highest density pulses have been selected because they are those with highest risk to be not limited by low-n modes. Figure 25(*a*) shows the stability diagram for the $A_{eff} = 2.5$ pulse. The pedestal is near the stability boundary and the most unstable modes have toroidal numbers in the range $n = 1 - 5$. A similar conclusion can be achieved for the highest density plasmas at $A_{eff} = 2.9$, whose stability diagram is shown in figure 25(*b*). In this case, the most unstable modes have toroidal numbers slightly higher, in the range $n = 3 - 7$. The eigenfunctions of both pulses are similar to those show in figure 11(*b*), with a clear peeling component.

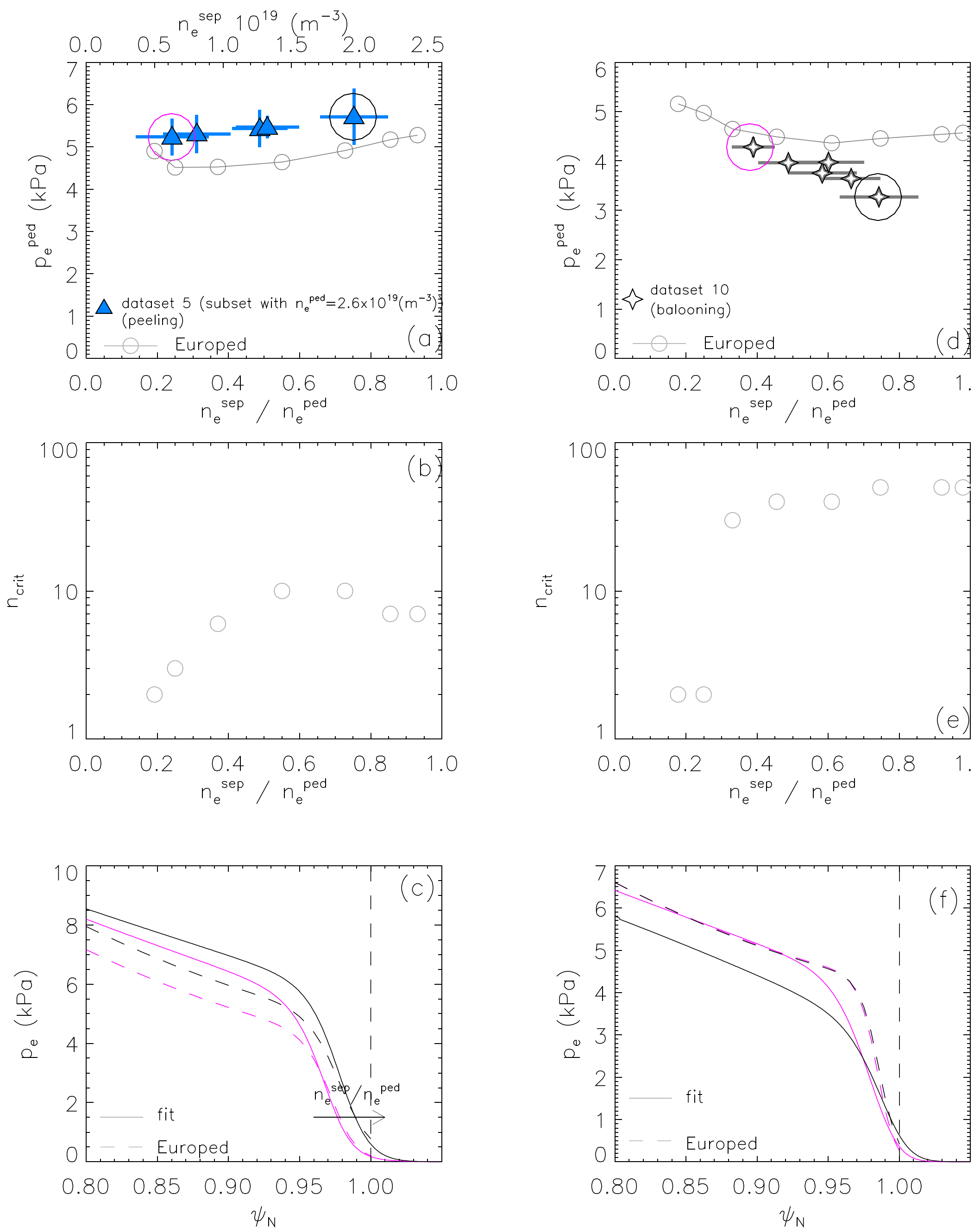

Figure 22. Correlation between p_e^{ped} and n_e^{sep}/n_e^{ped} for the peeling limited subset at $q_{95} = 8.5$ and $n_e^{ped} = 2.6 \times 10^{19} (\mathrm{m}^{-3})$ (*a*) and the ballooning limited dataset 10 [40]. (*b*) The triangles and the stars show the experimental data and the grey empty circles the Europed predictions. Frames (*b*) and (*e*) show the corresponding critical *n*, i.e. the predicted most unstable toroidal mode number. The pressure profiles (determined from the T_e fit and the n_e fit of figure 18) are shown as continuous lines in frame (*c*) and (*f*), while the Europed predicted profiles are shown as dashed lines. The profiles correspond to the data highlighted with a circle in frame (*a*) and frame (*d*).

The effect of the isotope mass on the pedestal height is shown in figure 26 for datasets 5 (deuterium), 6 (mixed D/T) and 7 (tritium-rich). The increase of the isotope mass leads to a clear increase in n_e^{ped}, whose maximum value increases from $n_e^{ped} \approx 2.6 \times 10^{19} \left(\mathrm{m}^{-3}\right)$ for the deuterium dataset to $n_e^{ped} \approx 3.0 \times 10^{19} \left(\mathrm{m}^{-3}\right)$ in the T-rich dataset. No effect is observed on the pedestal height of the electron temperature, which remains in the range $T_e^{ped} \approx 1.3 - 1.5\mathrm{keV}$. A similar conclusion is achieved for the ion temperature. As a consequence, the pedestal pressure increases with the increasing isotope mass. The positive correlation between p_e^{ped} and n_e^{ped} in figure 26(*b*) is very similar for all the three values of A_{eff}.

The gradients are shown in figure 27. The pressure gradient reaches a higher value in the T-rich dataset. This increase is not due to a change in the temperature gradient, as ∇T_e does

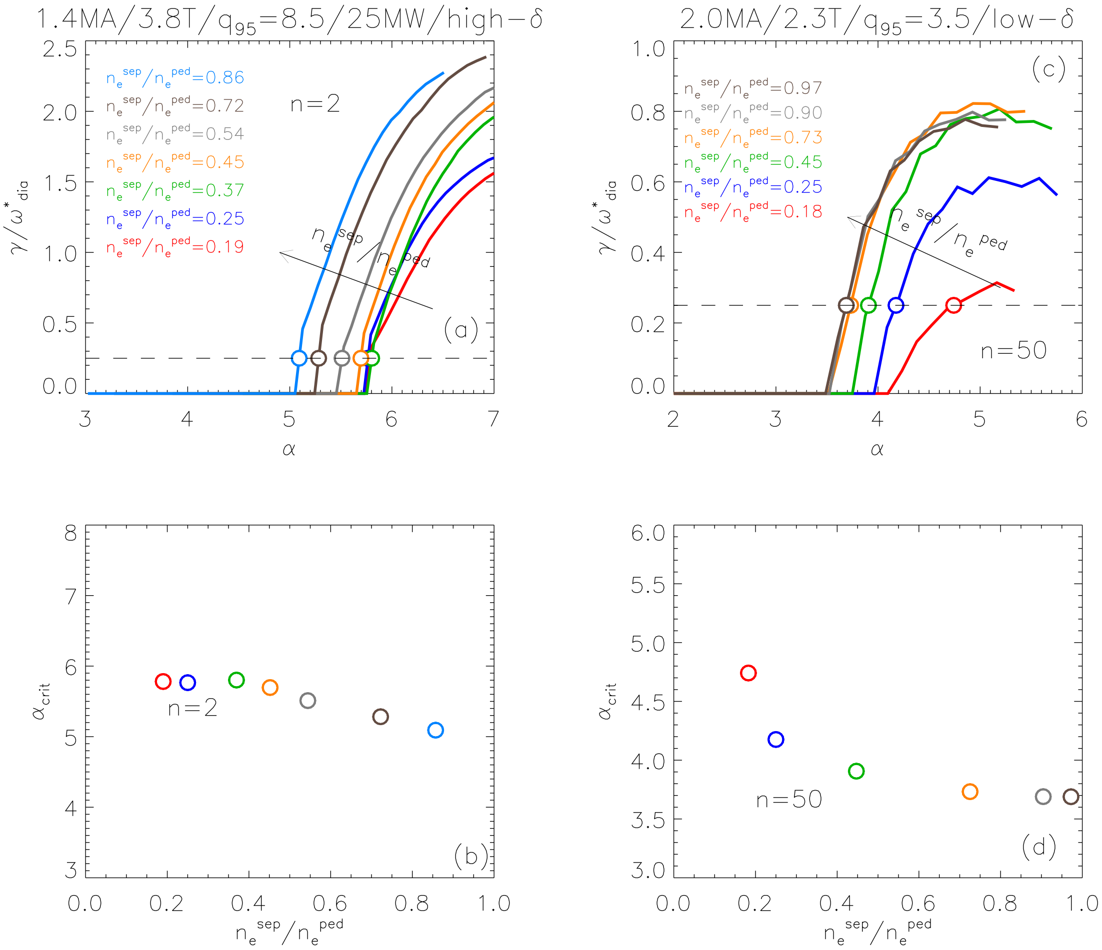

Figure 23. (*a*) Growth rates versus normalized pressure gradient of the $n = 2$ peeling mode for the Europed modeling of figure 22(*a*). Frame (*b*) shows the corresponding critical pressure gradient versus n_e^{sep}/n_e^{ped}. Frame (*c*) and frame (*d*) show a similar analysis of the $n = 50$ ballooning mode for the Europed modeling of figure 22(*d*).

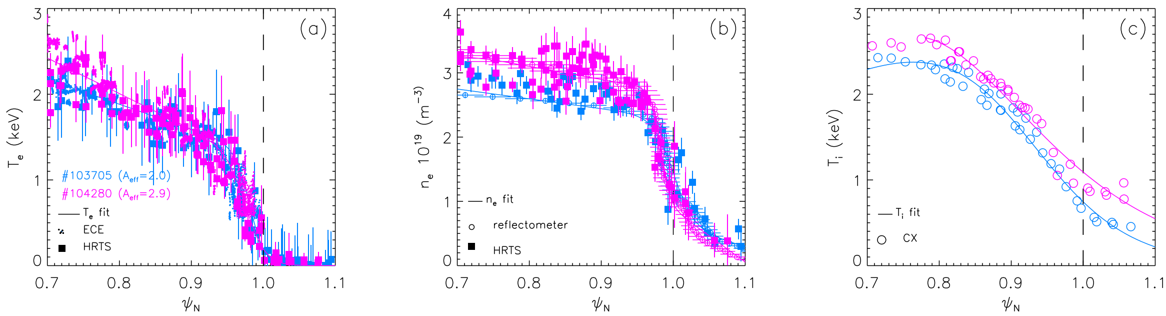

Figure 24. Comparison of the pre-ELM profiles of electron temperature (*a*), electron density (*b*) and ion temperature (*c*) at 1.4 MA/3.8 T, $q_{95} = 8.5$, 25 MW and gas rate $4 \times 10^{21}(\mathrm{e\ s}^{-1})$ for a pure deuterium pulse (blue) and a tritium-rich pulse (magenta). The symbols highlights the experimental pre-ELM profiles and the continuous lines the corresponding fits.

not shown any correlation with the isotope mass, figure 27(*b*). Instead, the increase in ∇p_e is due to an increase in the density gradient, as shown in figure 27(*c*). The gradients of the pressure and density are very well correlated with n_e^{ped}. No systematic difference in the trends can be observed between the pure deuterium dataset and the mixed deuterium/tritium dataset.

The pedestal width does not show any clear correlation with the isotope mass, as already observed in ballooning limited pedestals [66], and therefore it is not further discussed.

In conclusion, the plasma is limited by low-*n* peeling mode also using mixed deuterium/tritium as fuelling gas. The increase in A_{eff} leads to an increase in the pedestal pressure due to the increase in the pedestal density. The

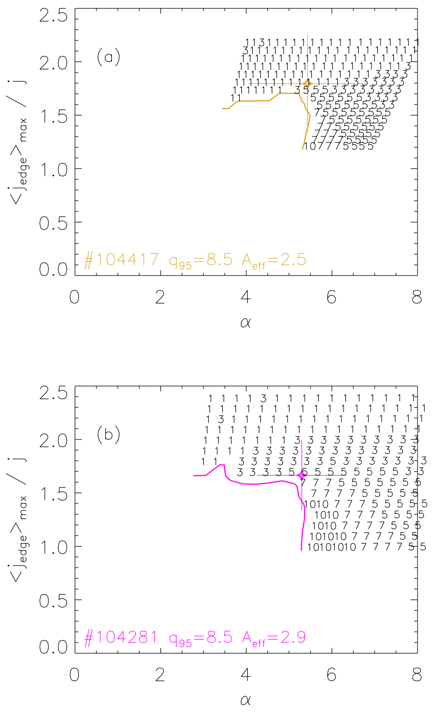

Figure 25. Pedestal stability for the (*a*) $A_{\rm eff} = 2.5$ pulse at highest density (gold) and the (*b*) $A_{\rm eff} = 2.9$ pulse at highest density (magenta). The thick lines highlight the stability boundary and the stars highlight the operational point. The numbers identify the most unstable mode.

increases in the pedestal heights are due mainly to the increases in the respective gradients. The correlations of $p_{\rm e}^{\rm ped}$ and $\nabla p_{\rm e}^{\rm ped}$ with $n_{\rm e}^{\rm ped}$ are very similar in deuterium and in mixed deuterium/plasmas.

6.2. Pedestal predictions of isotope mass effects in peeling limited plasmas and comparison with ballooning limited pedestals

The experimental trends between $p_{\rm e}^{\rm ped}$ and $\nabla p_{\rm e}^{\rm ped}$ versus $n_{\rm e}^{\rm ped}$ do not seem to be correlated to $A_{\rm eff}$. This suggests that the higher $p_{\rm e}^{\rm ped}$ achieved in the T-rich peeling limited dataset is due to the higher density and not to a direct effect of the isotope mass on the pedestal stability. To test this hypothesis, two sets of Europed predictions have been performed, assuming pure deuterium and assuming pure tritium plasmas. The input parameters for a pulse in deuterium at $q_{95} = 3.8$ have been used and then the Europed predictions have been repeated using different density. The pedestal predictions are shown as empty circles in figure 26 and in figure 27. Qualitatively, the predictions show a correlation consistent with the experimental data (figure 26). A reasonable qualitative agreement is obtained also for the pressure gradient and the density gradient (figure 27). The effect of the isotope mass on the predictions is negligible, as indeed expected with ideal MHD [65, 66].

The origin of the quantitative disagreement between predictions and experimental results at high density is unclear at the moment. The disagreement is likely correlated to the underestimated $\nabla T_{\rm e}^{\rm ped}$ at high density, figure 27(*b*), and it is in part related to the fact that the Europed $n_{\rm e}^{\rm ped}$ scans were performed with the other input parameters constant (while the variation of $n_{\rm e}^{\rm ped}$ is experimentally correlated to variations in $\beta_{\rm N}$, $T_{\rm i}/T_{\rm e}$ and relative shift).

A comparison of the effect of the isotope mass on the pedestal in high collisionality ballooning limited plasmas is shown in figure 28. The deuterium ballooning dataset (blue data) does not show any increase of $\nabla p_{\rm e}^{\rm ped}$ versus $n_{\rm e}^{\rm ped}$. The higher $A_{\rm eff}$ dataset has a higher $\nabla p_{\rm e}^{\rm ped}$ than the deuterium dataset. The behavior of $\nabla p_{\rm e}^{\rm ped}$ is therefore different from that of the low-n peeling dataset. While in the peeling dataset a clear positive correlation can be seen between $\nabla p_{\rm e}^{\rm ped}$ and $n_{\rm e}^{\rm ped}$ and no systematic difference in the trends is present for any $A_{\rm eff}$, in the ballooning dataset the correlation between ∇p_e^{ped} and n_e^{ped} is less clear and the change of the isotope mass leads to a significant increase in $\nabla p_{\rm e}^{\rm ped}$. To further highlight the difference, the empty circles in figure 28 show the Europed predictions of a density scan using as reference the lowest density ballooning limited pulse. The prediction shows a weak decrease of the pressure gradient with increasing $n_{\rm e}^{\rm ped}$. The predicted trend is opposite to the experimental trend. The disagreements are due to two reasons. First of all, the predicted decrease of $\nabla p_{\rm e}^{\rm ped}$ with increasing $n_{\rm e}^{\rm ped}$ is expected in ballooning limited pedestal, as shown in figure 16(*d*). Second, resistive MHD was necessary to explain the effect of the isotope mass in the ballooning limited deuterium pulses [66].

The picture that emerges is the following. In the peeling limited dataset, the increasing isotope mass leads to an increase in the density via the increase of the density gradient. This behavior is similar to that in ballooning limited plasmas. Then, the increasing $n_{\rm e}^{\rm ped}$ stabilizes the low-n modes (in way similar to what discussed in section 4). The stabilization of the low-n modes leads to the increase in the pedestal pressure gradient and hence in $p_{\rm e}^{\rm ped}$. In the peeling limited dataset, no direct effect of the isotope mass on the pedestal stability is clearly observed and the experimental results can be explained only by the stabilizing effect of the increased $n_{\rm e}^{\rm ped}$. The explanation of the effect of the isotope mass in the high-n ballooning limited plasmas is significantly different. The increase of the isotope mass still leads to an increase in the pedestal density via an increased density gradient. However, the increase of the density has a destabilizing effect on the high-n ballooning modes. As discussed in [66], the increase in $\nabla p_{\rm e}^{\rm ped}$ in high-n ballooning limited plasmas was a direct effect of $A_{\rm eff}$ on resistive MHD stability.

7. Discussion

This work has described the pedestal behavior in JET-ILW peeling limited plasmas and tested the capabilities of the Europed predictions. Peeling limited pedestals in JET-ILW have been achieved by operating at low density (using low

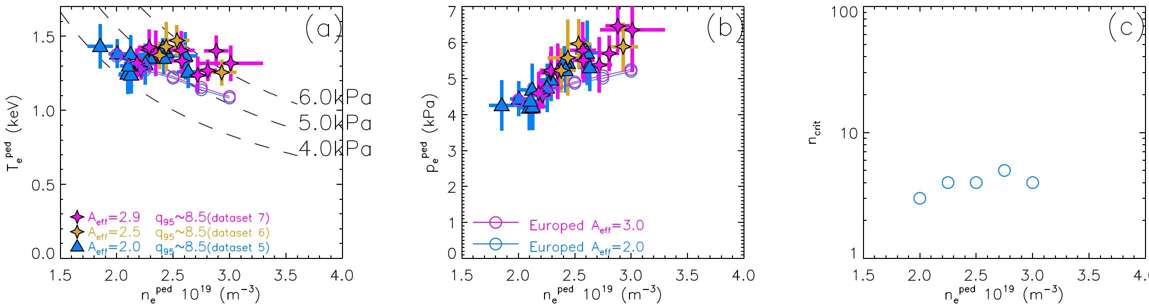

Figure 26. (*a*) Pedestal temperature versus electron pedestal density for the $q_{95} = 8.5$ datasets in pure deuterium (blue), mixed deuterium/tritium with $A_{\rm eff} = 2.5$ (gold) and tritium-rich with $A_{\rm eff} = 2.9$ (magenta) datasets. The full symbols highlights the electron temperature while the crosses highlight the ion temperature. Frame (*b*) shows the electron pedestal pressure versus $n_e^{\rm ped}$. The empty circles in frames (*a*) and (*b*) represents the Europed predictions discussed in section 6.2. Frame (*c*) shows the toroidal number of most unstable mode predicted by Europed.

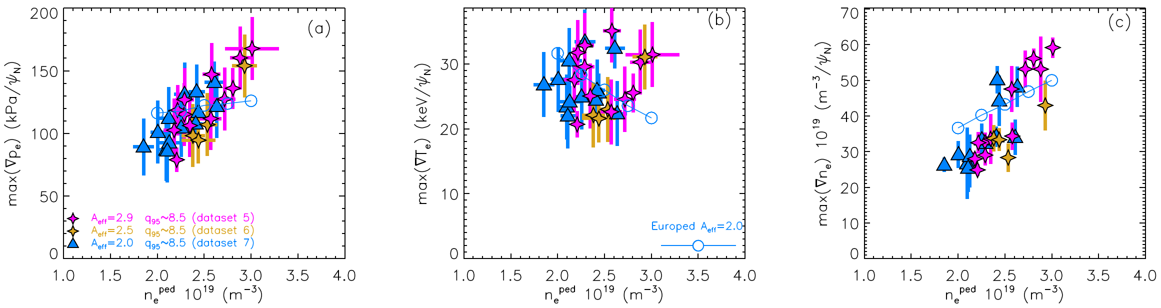

Figure 27. Correlation of the maximum pedestal electron pressure gradient (*a*), temperature gradient (*b*) and density gradient (*c*) with pedestal density for the $q_{95} = 8.5$ datasets in pure deuterium (blue), mixed deuterium/tritium with $A_{\rm eff} = 2.5$ (gold) and tritium-rich with $A_{\rm eff} = 2.9$ (magenta) datasets. The full symbols show the experimental data and the empty symbols the Europed predictions discussed in section 6.2.

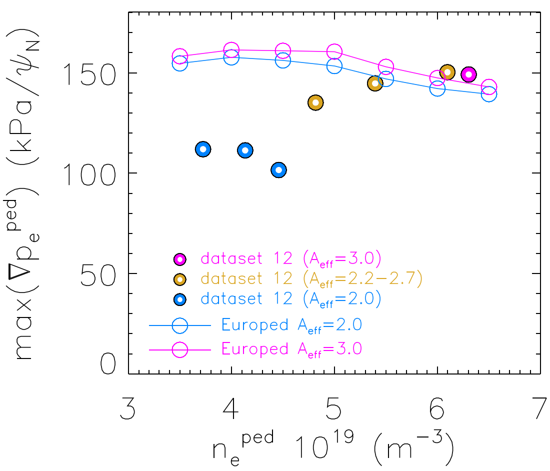

Figure 28. Maximum pressure gradient versus pedestal density for ballooning limited plasmas of dataset 12 and corresponding Europed predictions.

I_p and with the outer strike point near the pump duct), high temperature (using the highest possible auxiliary power compatible with the density range) and by stabilizing the ballooning modes using high q_{95} (reached by high B_t). As shown by the peeling-ballooning stability analysis and by the radial profile of the eigenfunctions, pedestals limited by peeling instabilities have been reached in the high q_{95} pulses.

Despite the pulses described in this work have a pedestal limited by peeling mode, the operational point remains close to the corner of the of the peeling-ballooning stability diagram. This is not considered a major issue for the conclusions. Indeed, the pedestal behavior in the plasmas achieved in this work is very different from that observed in the earlier ballooning limited JET-ILW pedestals. Moreover, some earlier works show that ITER is supposed to operate with a pedestal characterized by a stability very similar to that achieved in this work, with the operational point close to the nose of the stability diagram [7].

A key goal of the work was to validate pedestal predictions in peeling limited plasmas. This was done using the Europed code [64] with the EPED1 model implementation [4]. The validation was done with two steps. First, the model was used to understand how to operate to reach peeling limited pedestal in JET-ILW. This has guided us to build the strategy discussed in section 3.1. *A posteriori*, the comparison between the experimental results and the planned strategy has shown an optimal qualitative agreement with the predictions, as discussed in section 3.5. Second, once peeling limited pedestals have been achieved, a set of experimental scans have been performed in $n_e^{\rm ped}$, $n_e^{\rm sep}/n_e^{\rm ped}$ and $A_{\rm eff}$. The corresponding Europed predictions show a good qualitative agreement with the experimental data.

The Europed predictions have been performed by changing only the scanned parameter while keeping constant all other input parameters. This is not consistent with the actual plasma behavior, since in an experimental scan it is impossible to vary only one single parameter and variations in β_N, T_i/T_e and n_e^{sep} also occur. So it is impossible to expect a good quantitative agreement between this type of predictions and the experimental results. A different approach could have been to match all the input parameters to the experimental values for each single pulse. However, this different approach would not have been fully predictive. The approach of scanning a single parameter in Europed has the advantage of providing insights into the physics of peeling modes.

This work has also highlighted the importance of developing integrated modeling of SOL, pedestal and core. As mentioned above, several parameters used in the present Europed version are not predicted but are input parameters. While a self-consistent integrated core-pedestal model was tested in the past in Europed [79] and a model for n_e^{ped} predictions has been recently developed [81], the inclusion of the SOL (in particular the modeling of n_e^{sep}/n_e^{ped}) and of the behavior of T_i/T_e are not done yet.

In the datasets used in this work, the increase of the gas rate has led to a decrease in the pedestal density. We speculated that this correlation is due to the increase in the ELM particle losses and/or high SOL opacity, but further investigations are necessary to reach conclusive claims. A negative correlation between n_e^{ped} and gas rate might not be necessarily a characteristic of all peeling limited pedestals but it is more likely linked to the low n_e^{ped} and high n_e^{sep} ranges achieved and the high SOL opacity.

This work has focused on three key aspects, the description of the experimental pedestal structure, the pedestal stability and the comparison with the pedestal predictions. Further work is necessary to reach a better understanding of the pedestal physics in peeling limited plasmas. First of all, the pre-ELM experimental MHD activity can be investigated. Preliminary results [82] shows that low-*n* modes localized in the pedestal region appears in the pre-ELM phase. A comparison with the Europed predictions, shows a behavior qualitatively similar between n_{crit} and the measured pre-ELM low-*n* modes [82]. Characterization of the ELM losses needs also further investigation. ELM energy losses are supposed to increase with decreasing pedestal collisionality and ITER is expected to have $W_{ELM}/W_{ped} \approx 0.3$ [73]. Characterizing ELM energy and particle losses in the present low collisionality peeling limited pedestals will be an important result for ITER. Another topic that needs further investigation is the pedestal transport, both from the experimental and the modeling point in view. In particular, in the low collisionality range achieved in present work, the pedestal transport might be characterized by micro-instabilities significantly different from those identified in the medium-high collisionality ballooning limited JET-ILW pedestals. In earlier works, for example, the electron scale was characterized by ETG turbulence [40, 66, 83] and no KBM were identified.

Understanding of the effect of the isotope mass on the pedestal is an important point related to the pedestal transport. As discussed in section 6, both in medium-high collisionality ballooning limited pedestals and in the low collisionality peeling limited pedestals, the increase of the isotope mass has led to an increase of n_e^{ped} via an increase in the pedestal density gradient. In JET-ILW this effect seems to be general and occurs over a wide range of parameters and scenarios. Due to the lack of measurement of particle sources, it is impossible to experimentally conclude if the increase of ∇n_e with A_{eff} is due to a reduction of the pedestal particle transport or to an increase in the sources. Gyrokinetic analysis similar to that performed in earlier JET-ILW pulses in hydrogen and deuterium [84] would be important to clarify this issue.

An interesting results related to the effect of the isotope mass is that, despite the density behavior is very similar in peeling and ballooning pedestals, the mechanism that leads to the increased pedestal pressure with increasing A_{eff} seems very different between ballooning and peeling limited pedestals. In medium/high collisionality ballooning limited pedestals discussed in [66], the increase in the pedestal pressure was ascribed to the improvement in the pedestal stability with increasing A_{eff} when resistive MHD was used. The effect was very large because the deuterium pulses were characterized by low temperature and resistive MHD effects were not negligible. Instead, this mechanism is irrelevant in the low collisionality peeling limited plasma discussed in this work. Due to the high temperature achieved, resistive effects are negligible and ideal MHD is sufficient to describe the pedestal. With ideal MHD, the effect of the isotope mass on the stability is negligible [65, 66]. In the peeling limited pedestals discussed in this work, the increase of the pedestal pressure with increasing A_{eff} can be ascribed to an indirect effect of the isotope mass. The increase of the isotope mass leads to an increase of the pedestal density. In turn, being limited by peeling modes, the increase of the density stabilizes the pedestal leading to the increase of the pressure.

In this work, ideal MHD was sufficient to describe the pedestal stability. This might seem a contradiction with previous experimental and modeling results in JET-ILW [35, 42, 85] which emphasized the role of resistive MHD. However, the main datasets used in this work have reached significantly higher temperature than most of the previous JET-ILW plasmas, see for example figure 4(*e*). For comparison, figure 29 shows the resistivity calculated in the lower part of the pedestal for the main datasets used in this work (full triangles) and for all the earlier JET-ILW high-triangularity plasmas until 2020 (empty triangles). At high q_{95}, where the peeling limited scenario has been reached, the resistivity is a factor 3–4 lower than in the earlier datasets. It is therefore very reasonable that resistive MHD effects do not play a role in the main datasets discussed in this work.

The work has tried to experimentally reach ITER-relevant pedestal conditions in terms of collisionality, normalized Larmor radius and type of pedestal instabilities. Assuming the results can be qualitatively extrapolated to ITER, this work leads to two positive conclusions.

1. ITER is supposed to operate at high n_e^{sep}/n_e^{ped}. All earlier results, achieved in ballooning limited pedestals, show a

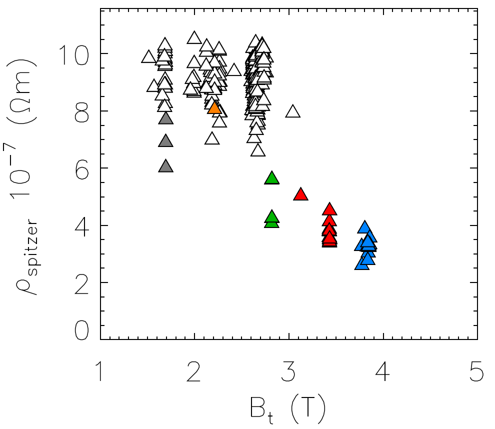

Figure 29. Spitzer resistivity versus the toroidal field for the main datasets (full triangles) and the JET-ILW high triangularity data until 2020 (dataset 11).

significant degradation of the pedestal pressure at high n_e^{sep}/n_e^{ped}. Instead, the present results achieved in peeling limited plasmas show that high n_e^{sep}/n_e^{ped} operation will not necessarily lead to a degraded pedestal pressure. However, the present results show that the increase in n_e^{sep}/n_e^{ped} can increase n_{crit}, suggesting that ballooning modes might be destabilized at very high n_e^{sep}/n_e^{ped} in ITER.

2. Operation in mixed deuterium/tritium plasmas in peeling limited scenarios leads to an improvement of the pedestal pressure. This is very promising for the future ITER operation.

8. Conclusions

This work has shown that JET-ILW can reach pedestals limited by peeling modes. This is the first time a metal wall machine has reached such conditions. This scenario has allowed to perform scans in plasma parameters that have been used to validate pedestal predictions in ITER-relevant conditions. Peeling limited pedestals have been achieved by operating at high q_{95}, therefore stabilizing ballooning modes. The experimental behavior of the q_{95} scan (obtained via a B_t scan) is in very good qualitative agreement with the predictive modeling. The density scan performed in the peeling limited plasmas has shown that the increasing density leads to an increased pedestal pressure. This is the expected behavior in peeling limited plasma and it is agreement with earlier DIII-D results [10]. Indeed, the pedestal predictions of the density scan are in reasonable agreement with the experimental behavior. The role n_e^{sep}/n_e^{ped} has been assessed. Both experimental results and predictions show that the pedestal pressure does not decrease with increasing n_e^{sep}/n_e^{ped}. The pedestal behavior in the density scan and in the n_e^{sep}/n_e^{ped} scan are significantly different from those in all earlier ballooning limited pedestals, where degradation of the pedestal was observed. Finally, the work has presented a unique dataset in mixed deuterium/tritium plasma in peeling limited pedestals. The result is very promising for ITER and shows an increase in the pedestal pressure with increasing isotope mass, due to the increased pedestal density.

This work has also highlighted that is necessary to further develop fully integrated core-pedestal-SOL modeling to have reliable pedestal predictions. Nonetheless, it has shown that the present pedestal predictions can qualitatively well describe the pedestal behavior approaching ITER-relevant conditions.

Acknowledgment

This research is supported by Vetenskapsrådet, under Grant Numbers 2023-04895. This scientific paper has been published as part of the international project co-financed by the Polish Ministry of Science and Higher Education within the programme called 'PMW' for 2024. This work has been carried out within the framework of the EUROfusion Consortium, funded by the European Union via the Euratom Research and Training Programme (Grant Agreement No 101052200—EUROfusion). Views and opinions expressed are however those of the author(s) only and do not necessarily reflect those of the European Union or the European Commission. Neither the European Union nor the European Commission can be held responsible for them.

Appendix A. Ion temperature at the pedestal and at the separatrix

The ion temperature behavior for the main datasets used in this work is shown in figure 30 for the deuterium plasmas discussed in sections 3–5. Another important effect of the gas rate variation is related to the ratio between T_i and T_e. The ratio T_i^{ped}/T_e^{ped} is shown in figure 30(*a*) and the ratio T_i^{sep}/T_e^{sep} in figure 30(*b*). Clear correlations with the gas rate can be seen. T_i^{ped}/T_e^{ped} decreases with increasing gas rate from ≈ 1.5 to ≈ 1.0. Also T_i^{sep}/T_e^{sep} has a clear negative correlation with the gas rate. The origin of the link between T_i/T_e cannot be ascribed to a variation in the electron-ion coupling, because the highest T_i/T_e ratios occur at low gas rate, so at higher density and higher collisionality than at high gas rate, see section 4. The reason for the variation in T_i/T_e in this dataset remains unclear. We can speculate that a possible reason is related to the change in f_{ELM}, with higher T_i achieved at lower gas rate and lower ELM frequency. The ion temperature at the pedestal top versus n_e^{ped} is shown in figure 30(*c*). T_i^{ped} increases with increasing density. The total pressure at the pedestal top versus n_e^{ped} is shown in figure 30(*d*). Also the total pressure show a positive correlation with n_e^{ped}. As discussed in section 4, this is a further confirmation that the main datasets studied in this work are limited by peeling instabilities rather than ballooning instabilities.

The ion temperature and the total pressure at the pedestal top for the n_e^{sep}/n_e^{ped} scan discussed in section 5 is shown in figure 31. The behavior of the total pressure and of the ion temperature versus n_e^{sep}/n_e^{ped} is qualitatively similar to that of the electrons (figure 19) and no strong correlation can be observed.

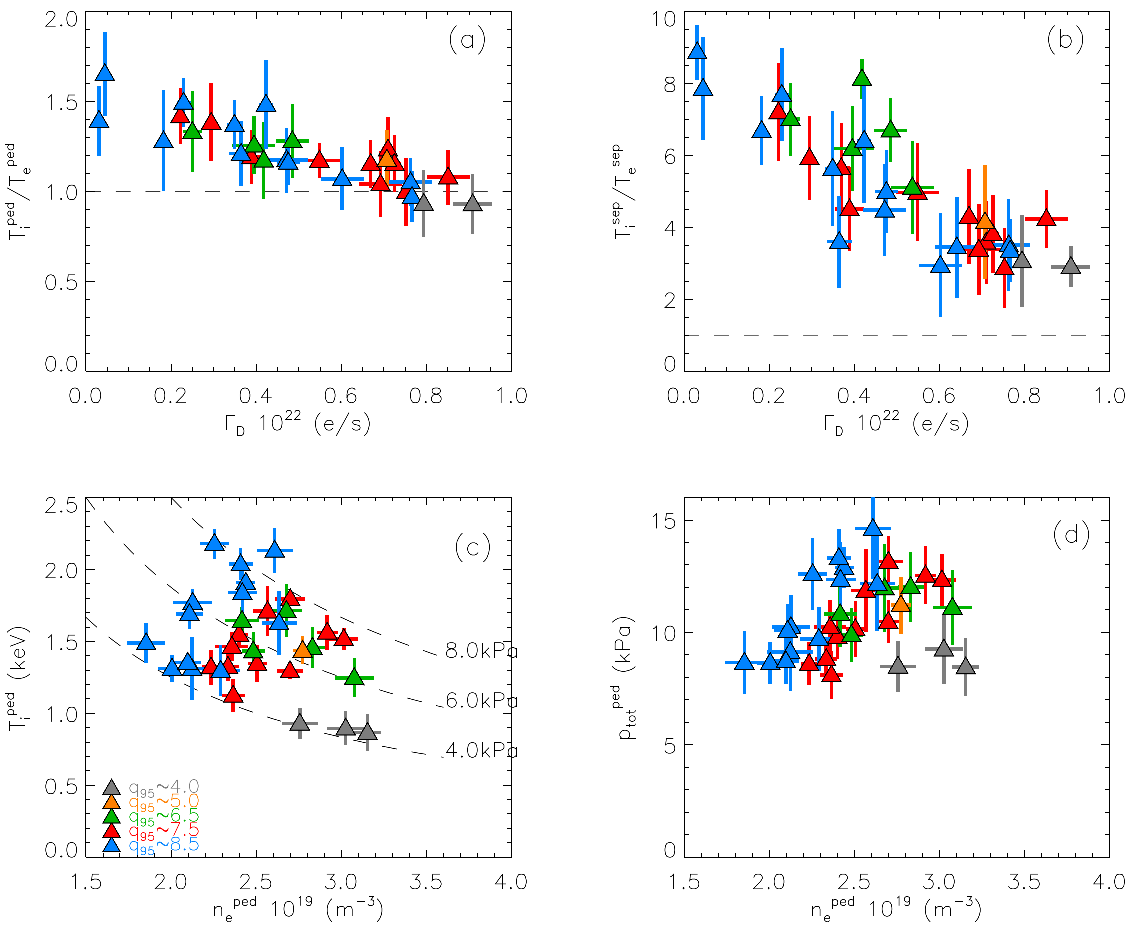

Figure 30. Ratio of ion to electron temperature versus gas rate at the pedestal top (*a*) and at the separatrix (*b*) for the gas scan datasets of section 4. Pedestal ion temperature and pedestal total pressure versus pedestal density for the gas scan datasets of section 4.

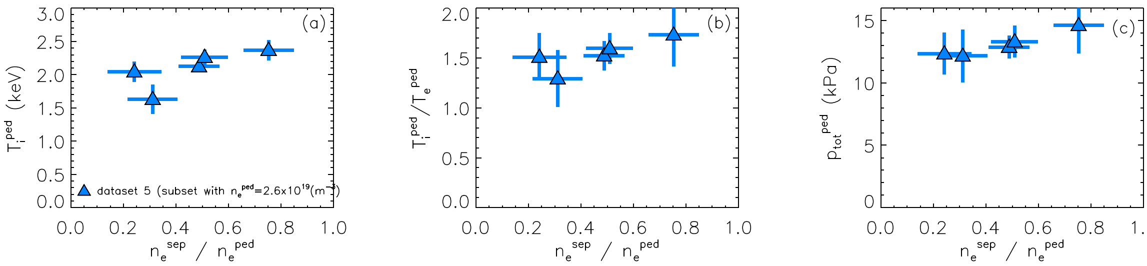

Figure 31. Pedestal height of total pressure (*a*) ion temperature (*b*) and ratio ion to electron temperature (*c*) versus $n_e{}^{sep}/n_e{}^{ped}$ for the subset at 1.4 MA/3.8 T, $q_{95} = 8.5$ and $n_e{}^{ped} = 2.6 \times 10^{19}(\mathrm{m}^{-3})$.

Appendix B. Sensitivity tests of Europed predictions

This appendix assesses the effect of the uncertainty in the input parameters on the conclusion of the work. Given the reasonable agreements between pedestal stability and Europed predictions, this assessment has been done using Europed.

An important parameter whose impact of the pedestal predictions has not been discussed much in the past is the ratio T_i/T_e. As shown figures 9(*c*) and (*b*) the common JET-ILW assumption $T_i = T_e$ is not valid for the datasets used in this work. Indeed, throughout the paper the stability analysis has been done using both the experimental pre-ELM T_e and T_i profiles and the Europed predictions have assumed $T_i^{ped} = 1.2T_e^{ped}$ and $T_i^{sep} = 4T_e^{sep}$. Therefore, figure 32 assesses the effect of T_i/T_e on the pedestal pressure predictions and on the toroidal mode number of the most unstable mode. The input parameters used are $I_p = 1.4$MA, $B_t = 3.8$T, high triangularity, $n_e^{ped} = 1.8 \times 10^{19}\left(\mathrm{m}^{-3}\right)$, $T_e^{sep} = 200$eV, zero relative shift, $\beta_N = 2.1, Z_{eff} = 1.5, A_{eff} = 2$ with toroidal mode numbers $n =$ 1, 2, 3, 4, 5, 6, 7, 10, 20, 30, 40, 50 included. These input parameters corresponds to the high density deuterium pulse of figure 15(*a*). The effect of T_i^{sep}/T_e^{sep} (assuming $T_i^{ped} = 1.2T_e^{ped}$) is shown in figure 32(*a*). The increase of T_i^{sep}/T_e^{sep} at

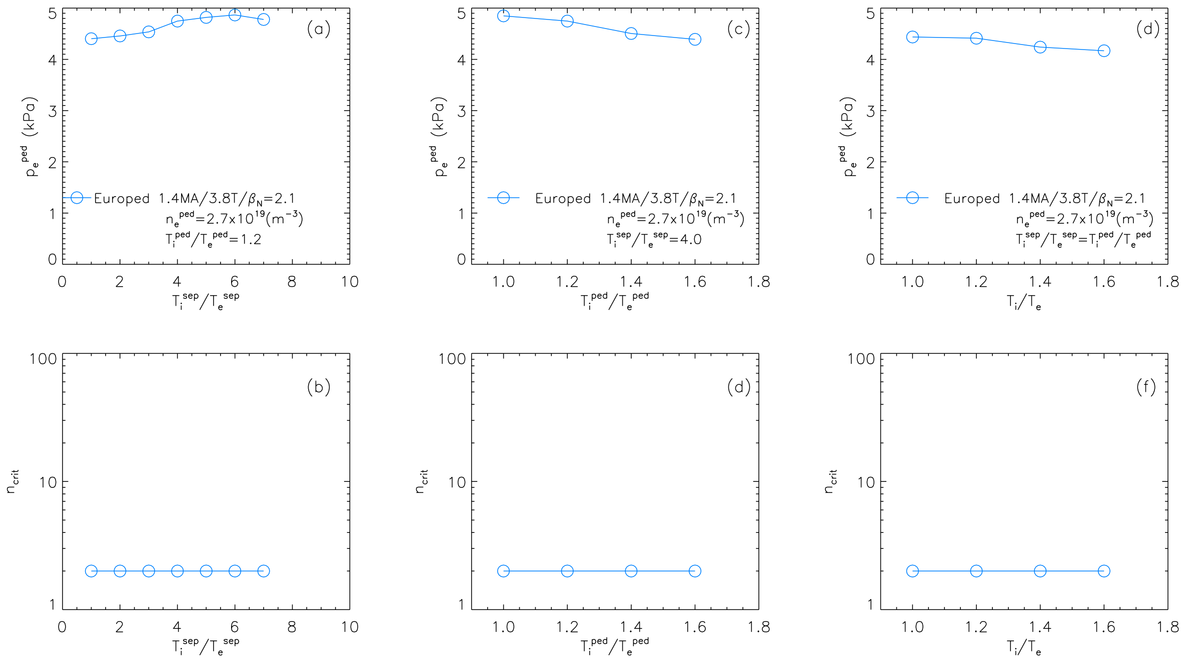

Figure 32. Europed sensitivity test of the effect of T_i/T_e on the predicted pedestal pressure height (top frames) and the predicted most unstable toroidal mode number (bottom frames). The input parameters used are $I_p = 1.4MA$, $B_t = 3.8T$, high triangularity, $n_e^{ped} = 1.8 \times 10^{19}\,(\mathrm{m}^{-3})$, $T_e^{sep} = 200\mathrm{eV}$, zero relative shift, $\beta_N = 2.1$, $Z_{eff} = 1.5$, $A_{eff} = 2$. The left frames shows the effect of T_i^{sep}/T_e^{sep} at constant T_i^{ped}/T_e^{ped}, the central frames shows the effect of T_i^{ped}/T_e^{ped} (assuming $T_i^{sep} = 4T_e^{sep}$), the right frames shows the effect of the simultaneous increase is T_i^{ped}/T_e^{ped} and T_i^{sep}/T_e^{sep}.

constant T_i^{ped}/T_e^{ped} reduces the gradient of the ion temperature which allows a higher T_e gradient to reach the critical pressure gradient. Indeed, figure 32(*a*) shows a weak increase in predicted electron pressure. However, despite the sensitivity test have been performed in the wide range $T_i^{sep}/T_e^{sep} = 1-7$ (corresponding to the experimental range shown in figure 9), the toroidal mode number of the most unstable mode remains $n = 2$, as shown in figure 32(*b*). The effect of T_i^{ped}/T_e^{ped} (assuming $T_i^{sep} = 4T_e^{sep}$) is shown in figure 32(*c*). The increase of T_i^{ped}/T_e^{ped} at constant T_i^{sep}/T_e^{sep} increases the T_i gradient therefore leading to a lower T_e gradient to reach the same critical pressure gradient. Indeed, figure 32(*c*) shows a weak reduction in predicted electron pressure. However, also in case the most unstable mode remains $n = 2$, as shown in figure 32(*d*). Finally, figure 32(*e*) show the effect of increasing simultaneously T_i^{ped}/T_e^{ped} and T_i^{sep}/T_e^{sep}. This lead to a weak reduction in the predicted pressure, but the most unstable mode is still $n = 2$.

Figure 33 assesses the effect of other important input parameters, T_e^{sep}, Z_{eff} and β_N. In all cases, the most unstable mode is a peeling instability characterized by $n < 4$. It is worth to mention that both T_e^{sep} and Z_{eff} have been varied over a wide range, larger than any possible uncertainty. This is important because the T_e^{sep} values used is this work were determined with the two-point model (figure 2) and not experimentally determined and because the experimental value of Z_{eff} is highly uncertain, as discussed in section 2.1. It is worth to mention that the increase in β_N suppresses the $n = 4$ mode and makes the $n = 1$ become more unstable, as shown in figure 33(*f*).

In conclusion, a set of sensitivity tests has been done on the most uncertain Europed input parameters. The results show that the pedestal remains limited by peeling modes despite the wide range of parameter used. Therefore, the qualitative conclusions of the paper cannot be affected by the uncertainty on these parameters.

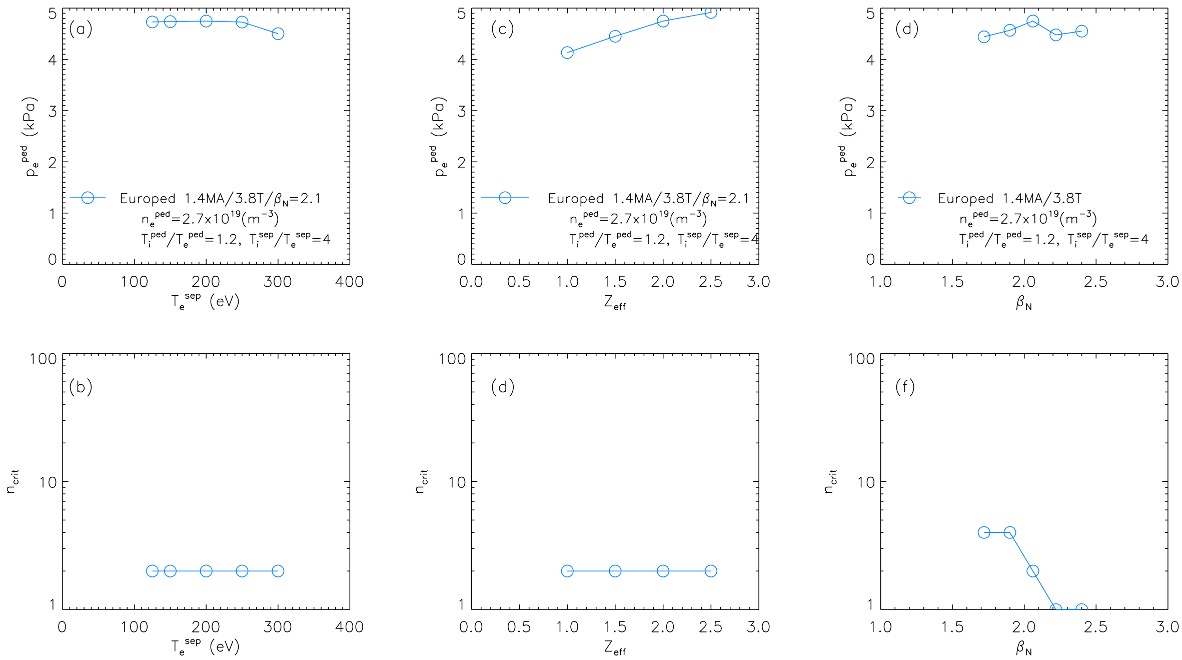

Figure 33. Europed sensitivity test of the effect of T_e^{sep} (left frames), Z_{eff} (central frames) and β_N (right frames) on the predicted pedestal pressure height (top frames) and the predicted most unstable toroidal mode number (bottom frames). The input parameters used are consistent with those of figure 32.

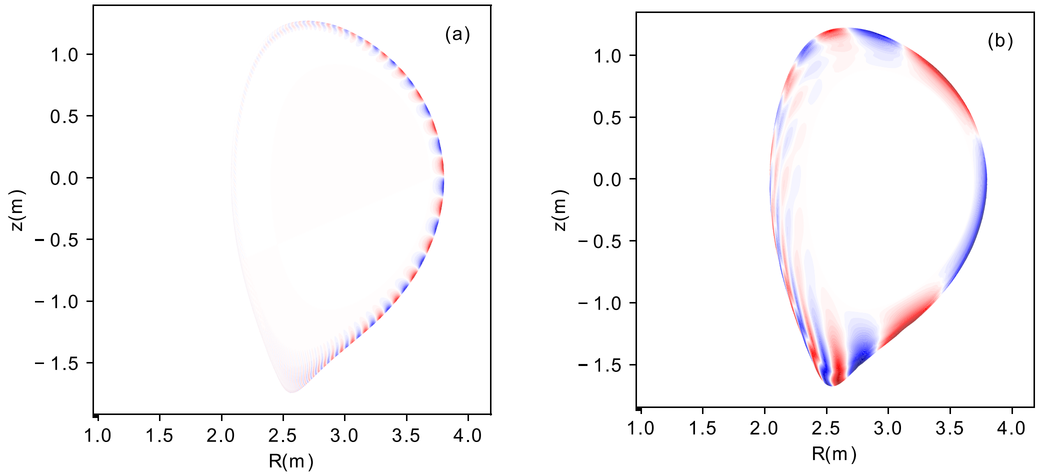

Figure 34. 2D reconstruction of the MHD radial displacement due to (*a*) the $n = 20$ mode corresponding to figure 6(*b*) and due to (*b*) the $n = 1$ mode corresponding to figure 6(*d*).

Appendix C. 2D radial displacement

This appendix complements the stability analysis of figures 6 and 11 by showing the 2D reconstructions of the of the MHD radial displacement for most unstable modes of some key examples.

Figure 34(*a*) shows the 2D reconstruction of the radial displacement for the $n = 20$ mode of the ballooning limited pedestal discussed in figures 6(*a*) and (*b*). A clear ballooning structure peaked at the low field side can be seen. Figure 34(*b*) shows the 2D reconstruction of the radial displacement for the $n = 1$ mode of the peeling limited pedestal discussed in figures 6(*c*) and (*d*). A peeling structure with the maximum amplitude near the X-point can be seen.

Figure 35(*a*) shows the 2D radial displacement for the $n = 1$ mode of the low density pedestal of figures 11(*a*) and (*b*). Figure 35(*b*) shows the displacement for the $n = 3$ mode of the high density pedestal of figures 11(*c*) and (*d*). The high density case shows that the ballooning component is not negligible.

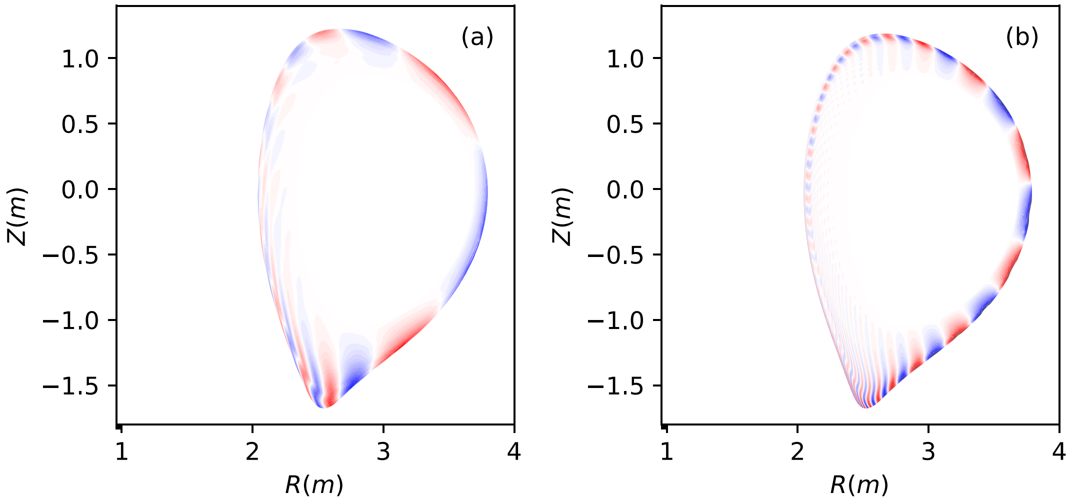

Figure 35. 2D reconstruction of the MHD radial displacement due to (*a*) the $n = 1$ mode corresponding to figure 11(*b*) and due to (*b*) the $n = 5$ mode corresponding to figure 11(*d*).

ORCID iDs

L. Frassinetti https://orcid.org/0000-0002-9546-4494
S. Saarelma https://orcid.org/0000-0002-6838-2194
C. Perez von Thun https://orcid.org/0000-0002-1166-2179
S. Wiesen https://orcid.org/0000-0002-3696-5475
A. Kappatou https://orcid.org/0000-0003-3341-1909
N. Vianello https://orcid.org/0000-0003-4401-5346
E. Alessi https://orcid.org/0000-0002-8750-9867
I.S. Carvalho https://orcid.org/0000-0002-2458-8377
B. Labit https://orcid.org/0000-0002-0751-8182
M. Maslov https://orcid.org/0000-0001-8392-4644
H. Nyström https://orcid.org/0000-0002-1310-4517
E. Pawelec https://orcid.org/0000-0003-1333-6331
G. Pucella https://orcid.org/0000-0002-9923-2770
D. Silvagni https://orcid.org/0000-0003-2103-3592
A. Stagni https://orcid.org/0000-0001-8084-1544
H.J. Sun https://orcid.org/0000-0003-0880-0013

References

[1] Kinsey J.E., Bateman G., Noun T., Kritz A.H., Pankin A., Staebler G.M. and Waltz R.E. 2003 *Nucl. Fusion* **43** 18451–4
[2] Sugihara M., Mukhovatov V., Polevoi A. and Shimada M. 2003 *Plasma Phys. Control. Fusion* **45** L55
[3] Snyder P.B., Wilson H.R., Ferron J.R., Lao L.L., Leonard A.W., Mossessian D., Murakami M., Osborne T.H., Turnbull A.D. and Xu X.Q. 2004 *Nucl. Fusion* **44** 320
[4] Snyder P.B., Groebner R.J., Leonard A.W., Osborne T.H. and Wilson H.R. 2009 *Phys. Plasmas* **16** 056118
[5] Snyder P.B. *et al* 2009 *Nucl. Fusion* **49** 085035
[6] Snyder P.B., Groebner R.J., Hughes J.W., Osborne T.H., Beurskens M., Leonard A.W., Wilson H.R. and Xu X.Q. 2011 *Nucl. Fusion* **51** 103016
[7] Saarelma S., Casper T., Chapman I.T., Huijsmans G.T.A., Kwon O., Lee J. and Loarte A. 2012 *Nucl. Fusion* **52** 103020
[8] Meneghini O. *et al* 2016 *Phys. Plasmas* **23** 042507
[9] Maget P., Artaud J.-F., Bécoulet M., Casper T., Faustin J., Garcia J., Huijsmans G.T.A., Loarte A. and Saibene G. 2013 *Nucl. Fusion* **53** 093011
[10] Snyder P.B. *et al* 2015 *Nucl. Fusion* **55** 083026
[11] Leonard A.W., Groebner R.J., Osborne T.H. and Snyder P.B. 2008 *Phys. Plasmas* **15** 056114
[12] Snyder P.B. *et al* 2007 *Nucl. Fusion* **47** 961–8
[13] Aiba N., Chen X., Osborne T.H., Honda M., Burrell K.H. and Snyder P.B. 2020 *Nucl. Fusion* **60** 092005
[14] Boyle D.P., Maingi R., Snyder P.B., Manickam J., Osborne T.H., Bell R.E. and LeBlanc B.P. 2011 *Plasma Phys. Control. Fusion* **53** 105011
[15] Groebner R.J. *et al* 2013 *Nucl. Fusion* **53** 093024
[16] Kleiner A., Ferraro N.M., Diallo A. and Canal G.P. 2021 *Nucl. Fusion* **61** 064002
[17] Kleiner A., Ferraro N.M., Canal G., Diallo A. and Maingi R. 2022 *Nucl. Fusion* **62** 076018
[18] Hughes J.W. *et al* 2018 *Nucl. Fusion* **58** 112003
[19] Meier L., Hoelzl M., Cathey A., Huijsmans G., Viezzer E., Dunne M., van Dijk J., Cruz Zabala D.J., Lackner K. and Günter S. 2023 *Nucl. Fusion* **63** 086026
[20] Beurskens M. *et al* 2013 *Nucl. Fusion* **53** 013001
[21] Beurskens M.N.A. *et al* 2009 *Plasma Phys. Control. Fusion* **51** 124051
[22] Leyland M.J. *et al* 2013 *Nucl. Fusion* **53** 083028
[23] Dunne M. *et al* 2017 *Plasma Phys. Control. Fusion* **59** 014017
[24] Dunne M. *et al* 2017 *Plasma Phys. Control. Fusion* **59** 025010
[25] Sheikh U., Dunne M., Frassinetti L., Blanchard P., Duval B.P., Labit B., Merle A., Sauter O., Theiler C. and Tsui C. 2019 *Plasma Phys. Control. Fusion* **61** 014002
[26] Frassinetti L. *et al* 2019 *Nucl. Fusion* **59** 076038
[27] Saarelma S., Hender T.C., Kirk A., Meyer H. and Wilson H.R. (MAST Team) 2007 *Plasma Phys. Control. Fusion* **49** 31
[28] Smith S.F., Kirk A., Chapman-Oplopoiou B., Clark J.G., Ham C.J., Horvath L., Maggi C.F., Scannell R. and Saarelma S. 2022 *Plasma Phys. Control. Fusion* **64** 045024
[29] Knolker M., Osborne T., Belli E., Henderson S., Kirk A., Kogan L., Saarelma S. and Snyder P.B. 2021 *Nucl. Fusion* **61** 046041
[30] Aiba N., Furukawa M., Hirota M., Oyama N., Kojima A., Tokuda S. and Yagi M. 2011 *Nucl. Fusion* **51** 073012
[31] Mossessian D.A. *et al* 2003 *Phys. Plasmas* **10** 1720–6
[32] Hughes J.W. *et al* 2013 *Nucl. Fusion* **53** 043016
[33] Beurskens M. *et al* 2014 *Nucl. Fusion* **54** 043001
[34] Saarelma S. *et al* 2015 *Phys. Plasmas* **22** 056115

[35] Maggi C. *et al* 2015 *Nucl. Fusion* **55** 113031
[36] Aiba N. *et al* 2017 *Nucl. Fusion* **57** 126001
[37] Giroud C. *et al* 2015 *Plasma Phys. Control. Fusion* **57** 035004
[38] Aiba N. *et al* 2018 *Nucl. Fusion* **60** 014032
[39] Frassinetti L. *et al* 2017 *Plasma Phys. Control. Fusion* **59** 014014
[40] Frassinetti L. *et al* 2021 *Nucl. Fusion* **61** 126054
[41] Wang H.Q. *et al* 2018 *Nucl. Fusion* **58** 096014
[42] Frassinetti L. *et al* 2021 *Nucl. Fusion* **61** 016001
[43] Garzotti L. *et al* 2019 *Nucl. Fusion* **59** 026006
[44] Imada K., Osborne T.H., Saarelma S., Clark J.G., Kirk A., Knolker M., Scannell R., Snyder P.B., Vincent C. and Wilson H.R. 2024 *Nucl. Fusion* **64** 086002
[45] Frassinetti L.*et al* 2022 Pedestal structure and stability at low collisionality in TCV *48th EPS Conf. Plasma Physics (27 June–1 July 2022, Maastricht, The Netherlands)* p O4.108 (available at: https://lac913.epfl.ch/epsppd3/2022/pdf/O4.108.pdf)
[46] Frassinetti L.*et al* 2022 Peeling limited pedestal experiments in JET-ILW and MAST-U *50th EPS Conf.Plasma Physics (8–12 July 2024, Salamanca, Spain)* P1.049 (available at: https://lac913.epfl.ch/epsppd3/2024/html/PDF/P1-049.pdf)
[47] Pasqualotto R., Nielsen P., Gowers C., Beurskens M., Kempenaars M., Carlstrom T. and Johnson D. 2004 *Rev. Sci. Instrum.* **75** 3891
[48] Bartlett D.V., Costley A.E., Porte L., Prentice R., Salmon N.A. and Sips G. 1990 *J. Nucl. Mater.* **176–177** 1064–9
[49] Réfy D.I., Brix M., Gomes R., Tál B., Zoletnik S., Dunai D., Kocsis G., Kálvin S. and Szabolics T. 2018 *Rev. Sci. Instrum.* **89** 043509
[50] Morales R.B. *et al* 2024 *Rev. Sci. Instrum.* **95** 043501
[51] King D. *et al* 2020 *Nucl. Fusion* **60** 096030
[52] Maslov M. *et al* 2023 *Nucl. Fusion* **63** 112002
[53] Frassinetti L., Beurskens M.N.A., Scannell R., Osborne T.H., Flanagan J., Kempenaars M., Maslov M., Pasqualotto R. and Walsh M. 2012 *Rev. Sci. Instrum.* **83** 013506
[54] Szepesi G. *et al* 2021 Advanced equilibrium reconstruction for JET with EFIT++ *47th EPS Conf. Plasma Physics (21–25 June 2021, Stiges, Spain)* P 3.1037 (available at: http://ocs.ciemat.es/EPS2021PAP/pdf/P3.1037.pdf)
[55] Groebner R.J. *et al* 2001 *Nucl. Fusion* **41** 1789
[56] Frassinetti L. *et al* 2017 *Nucl. Fusion* **57** 016012
[57] Haskey S.R., Grierson B.A., Stagner L., Burrell K.H., Chrystal C., Groebner R.J., Ashourvan A. and Pablant N.A. 2017 *JINST* **12** C10013
[58] Stangeby P.C., Canik J.M., Elder J.D., Lasnier C.J., Leonard A.W., Eldon D., Makowski M.A., Osborne T.H. and Grierson B.A. 2015 *Nucl. Fusion* **55** 093014
[59] Silvagni D. *et al* 2025 *Nucl. Mat. Energy* **42** 101867
[60] Huysmans G.T.A. *et al* 1991 *CP90—Conf. on Computational Physics* (*Amsterdam, 10–13 September 1990*) p 371
[61] Redl A., Angioni C., Belli E. and Sauter O. 2021 *Phys. Plasmas* **28** 022502
[62] Mikhailovskii A.B. *et al* 1997 *Plasma Phys. Rep.* **23** 844
[63] Miller R.L., Chu M.S., Greene J.M., Lin-Liu Y.R. and Waltz R.E. 1998 *Phys. Plasmas* **5** 973
[64] Saarelma S., Challis C.D., Garzotti L., Frassinetti L., Maggi C.F., Romanelli M. and Stokes C. 2018 *Plasma Phys. Control. Fusion* **60** 014042
[65] Horvath L. *et al* 2021 *Nucl. Fusion* **61** 046015
[66] Frassinetti L. *et al* 2023 *Nucl. Fusion* **63** 112009
[67] Dudson B.D., Umansky M.V., Xu X.Q., Snyder P.B. and Wilson H.R. 2009 *Comput. Phys. Commun.* **180** 1467
[68] Xu X.Q., Dudson B., Snyder P.B., Umansky M.V. and Wilson H. 2010 *Phys. Rev. Lett.* **105** 175005
[69] Challis C. *et al* 2015 *Nucl. Fusion* **55** 053031
[70] Leyland M.J. *et al* 2015 *Nucl. Fusion* **55** 013019
[71] Perez von Thun C. *et al* 2019 *Nucl. Fusion* **59** 056004
[72] Zohm H. *et al* 1996 *Plasma Phys. Control. Fusion* **38** 105
[73] Loarte A. *et al* 2003 *Plasma Phys. Control. Fusion* **45** 1549
[74] Tolman E.A., Hughes J.W., Wolfe S.M., Wukitch S.J., LaBombard B., Hubbard A.E., Marmar E.S., Snyder P.B. and Schmidtmayr M. 2018 *Nucl. Fusion* **58** 046004
[75] Urano H. *Proc. 43rd EPS Conf. on Plasma Physics* (*Leuven, Belgium, 4–8 July, 2016*) (available at: https://info.fusion.ciemat.es/OCS/EPS2016PAP/pdf/O4.121.pdf) p 4.121
[76] Schneider P.A., Wolfrum E., Groebner R.J., Osborne T.H., Beurskens M.N.A., Dunne M.G., Kurzan B., Pütterich T. and Viezzer E. 2013 *Nucl. Fusion* **53** 073039
[77] Mordijck S. 2020 *Nucl. Fusion* **60** 082006
[78] Mordijck S. *et al* 2024 *Nucl. Fusion* **64** 126034
[79] Saarelma S., Frassinetti L., Bilkova P., Challis C.D., Chankin A., Fridström R., Garzotti L., Horvath L. and Maggi C.F. 2019 *Phys. Plasmas* **26** 072501
[80] Schneider P.A. *et al* 2023 *Nucl. Fusion* **63** 112010
[81] Saarelma S. *et al* 2024 *Nucl. Fusion* **64** 076025
[82] Giovannozzi E.*et al* 2022 Low frequency intra ELM pedestal MHD activity observed in low collisionality peeling limited scenario on JET *50th EPS Conf. Plasma Physics (8–12 July 2024, Salamanca, Spain)* P 1.041 (available at: https://lac913.epfl.ch/epsppd3/2024/html/PDF/P1-041.pdf)
[83] Chapman B. *et al* 2022 *Nucl. Fusion* **62** 086028
[84] Predebon I., Hatch D.R., Frassinetti L., Horvath L., Saarelma S., Chapman-Oplopoiou B., Görler T. and Maggi C.F. 2023 *Nucl. Fusion* **63** 036010
[85] Nyström H., Frassinetti L., Saarelma S., Huijsmans G.T.A., Perez von Thun C., Maggi C.F., Hillesheim J.C. and contributors J. 2023 *Nucl. Fusion* **62** 126045